JOURNAL OF GEOPHYSICAL RESEARCH, VOL. 103, NO. A4, PAGES 6871-6889, APRIL 1, 1998

Generalized kinetic description of a plasma in an arbitrary field-aligned potential energy structure

G. V. Khazanov,[1,2] M. W. Liemohn,[3] E.N. Krivorutsky,[1] and T. E. Moore[4]

Abstract. We present a general solution to the collisionless Boltzmann (Vlasov) equation for a free-flowing plasma along a magnetic field line using Liouville's theorem, allowing for an arbitrary field-aligned potential energy structure including nonmonotonicities. The constraints of the existing collisionless kinetic transport models are explored, and the need for a more general approach to the problem of self-consistent potential energy calculations is described. Then a technique that handles an arbitrary potential energy distribution along the field line is presented and discussed. For precipitation of magnetospherically trapped hot plasma, this model yields moment calculations that vary by up to a factor of 2 for various potential energy structures with the same total potential energy drop. The differences are much greater for the high-latitude outflow scenario, giving order of magnitude variations depending on the shape of the potential energy distribution. Self-consistent calculations for the photoelectron-driven polar wind are compared with previous results, and it is shown that even a photoelectron concentration of 0.03% at the base of the simulation (500 km) will cause the potential energy distribution to violate the constraints of the existing models.

1. Introduction

When potential energy structures are the dominant factors influencing the evolution of the plasma distribution function, the collisionless Boltzmann (Vlasov) equation is commonly used in modeling the plasma behavior. This approach has broad applications across many disciplines: in near-Earth space for describing the hot plasma along inner magnetospheric field lines, in high-latitude ionospheric outflows, and for other situations involving a field-aligned potential difference; for rotating planetary magnetospheres to determine the effects of the centrifugal force; in astrophysics for describing objects such as pulsars; for modeling the solar wind acceleration region; and in laboratory plasmas to describe collisionless expansion into a vacuum.

The collisionless kinetic description has been used for many scenarios in near-Earth space. Models of this type have been used for the description of the hot plasma along an inner magnetospheric field line [*Alfvén and Fälthammar*, 1963; *Persson*, 1963; *Eviatar et al.*, 1964; *Whipple*, 1977; *Chiu and Schulz*, 1978; *Serizawa and Sato*, 1984; *Stasiewicz*, 1985; *Miller and Khazanov*, 1993; *Olsen et al.*, 1994], for planetary magnetospheres [*Lemaire*, 1976; *Huang and Birmingham*, 1992], and for high-latitude outflow and precipitation [*Lemaire and Scherer*, 1970; *Knight*, 1973; *Barakat and Schunk*, 1984; *Washimi and Katanuma*, 1986; *Pierrard and Lemaire*, 1996; *Khazanov et al.*, 1997; *Wilson et al.*, 1997]. They all have the same basic approach of knowing the distribution function at some reference altitude and then mapping this distribution along the field line according to a given or calculated potential energy structure.

Alfvén and Fälthammar [1963] were the first to study the generation of an electrostatic potential structure due to trapped particles in a magnetic mirror (magnetic flux tube). They demonstrated that an anisotropic collisionless plasma in a magnetic field can be in quasineutral equilibrium without a parallel electric field only if the magnetic field is homogeneous or if the pitch angle anisotropy is the same for both electrons and ions. They considered a single particle approach and determined that the electrostatic potential energy difference between the ionosphere and equator is of the order of the magnetic field mirror ratio multiplied by the mean perpendicular particle energy. For a typical mirror ratio ($\gamma \approx 40$ for an L shell of 4 and an altitude of 2000 km), the potential energy determined by *Alfvén and Fälthammar* [1963] can be well in excess of the total kinetic energy of the trapped plasma which creates this potential difference.

In steady state, *Persson* [1963] evaluated the particle distribution function using Liouville's theorem and confirmed the results of *Alfvén and Fälthammar* [1963]. However, *Persson* [1963] never computed the total electrostatic potential necessary for quasineutrality when the electrons and ions have different anisotropies. *Whipple* [1977] considered a generalization of the work by *Alfvén and Fälthammar* [1963]. The integral formalism of *Whipple* [1977], using a delta function for the trapped plasma at the equator, reproduces the results of *Alfvén and Fälthammar* [1963]; however, the electric potential, due to a variety of trapped distributions (in the absence of other plasma sources), was not investigated and compared with the *Alfvén and Fälthammar* [1963] model. *Chiu and Schulz* [1978] considered a self-consistent treatment for the electro-

[1]Center for Space Physics and Aeronomic Research, The University of Alabama in Huntsville.

[2]Now at the Geophysical Institute, Physics Department, University of Alaska Fairbanks.

[3]Space Sciences Laboratory, NASA Marshall Space Flight Center, Huntsville, Alabama.

[4]Laboratory for Extraterrestrial Physics, NASA Goddard Space Flight Center, Greenbelt, Maryland.

Paper number 97JA03436.
0148-0227/98/97JA-03436$09.00

static potential; however, their analysis included ionospheric plasma extracted upward by parallel electrostatic fields and backscattered electrons. *Chiu and Schulz* [1978] state that the *Alfvén and Fälthammar* [1963] model would produce unrealistically large potential drops (of the order of several hundred keV), but they never discuss the validity of the *Alfvén and Fälthammar* [1963] model. They do, however, mention that the large electric potentials would decrease in the presence of ionospheric plasma. *Chiu and Schulz* [1978] found potential drops of the order of the plasma kinetic energy. They derived accessibility criteria that quantify the limits of validity of their results, and the smoothness imposed by these constraints prohibits double layers or electrostatic shocks to form. Also, it is unclear from their analysis as to the magnitude of the electrostatic potential in the absence of ionospheric plasma and backscattered electrons. This last issue has been addressed by *Miller and Khazanov* [1993].

For ion outflows, the first description was the polar exosphere model of *Lemaire and Scherer* [1970, 1971, 1972], which used a Maxwellian distribution function instead of a single particle trajectory, allowing for infinite mirror points for the incoming (precipitating) particles. They present a full description of the possible trajectories of particles (ballistic, escaping, trapped, etc.) and calculate the densities, particle and energy fluxes, and pressures for each of these classes along the field line. This model has continued to be used since this time and was recently extended for the solution of a Lorentzian (kappa) distribution function instead of a Maxwellian distribution function [*Pierrard and Lemaire*, 1996].

A similar approach was used by *Knight* [1973], who calculated the field-aligned potential from a zero current assumption. He also limits the solution to a monotonic potential distribution from the plasma sheet to the ionosphere, and the resulting equations only depend on the beginning reference point for that population and the local spatial point. He also gives a similar analysis of the various regions of existence in velocity space for different populations along the field line. An important development here and by *Lemaire and Scherer* [1973, 1974] was the use of different distribution functions for the various regions, allowing for the self-consistent calculation of widely disparate plasma populations, such as the precipitating plasma sheet particles and the ionospheric outflow. Results similar to *Knight* [1973] except for a partially filled loss cone distribution for the trapped population were obtained by *Stasiewicz* [1985], and the result readily reduces to Knight's formula.

The model of *Olsen et al.* [1994], which calculated the generation of a self-consistent potential due to warm plasmaspheric plasma, took into account only the local spatial point in defining the filled integration region, thus filling in any low-energy holes in the distribution function due to drops in the potential energy. As mentioned in that study, this implies some scattering mechanism is filling in these holes. While it might be reasonable to assume that such holes will be filled in for low-energy populations (up to a few eV temperature), the scattering is inconsistent with the use of the Vlasov equation. A similar assumption was probably made by *Huang and Birmingham* [1992], because the formulation is the same except for a more generalized potential energy. Similarly, the Heaviside step function introduced in the distribution function by *Miller and Khazanov* [1993] to keep the total energy greater than zero is also inconsistent with the Vlasov equation because it is the kinetic energy of the particle that has this constraint.

Two recent models [*Khazanov et al.*, 1997; *Wilson et al.*, 1997] combine a Vlasov equation solution for the ions and photoelectrons with a hydrodynamic description for the thermal electrons for calculating polar wind outflows. Although it is a mixture of collisionless and collision-dominated treatments, this is applicable here because the ionospheric thermal electrons are much more collisional than the outflowing ions or hot populations. While both models use a kinetic formulation similar to that of *Lemaire and Scherer* [1970], their hydrodynamic approaches are different. For the thermal electrons, *Khazanov et al.* [1997] use the momentum and energy equations for the density and temperature and a zero current assumption to find the velocity along the field line, while *Wilson et al.* [1997] use a Boltzmann distribution for the density, which assumes no velocity and isothermal temperature, and then use a zero current condition at some altitude to generate a large potential barrier, reducing the large upward photoelectron flux.

A common trait of the models mentioned above is that they all depend only on the final position of the particles in space. The assumed accessibility of these particles to this point introduces a constraint on the functional dependence of the potential energy with respect to the magnetic field, which was recognized and discussed for the first time in detail by *Chiu and Schulz* [1978]. By considering only the electrostatic potential φ, they found two constraints on its derivatives with respect to the magnetic field B,

$$d\varphi/dB > 0 \tag{1}$$

$$d^2\varphi/dB^2 \le 0 \tag{2}$$

meaning that the electrostatic potential must increase smoothly from the point of minimum B, with a smoothly decreasing growth rate. These constraints must be satisfied by the potential energy when using any of the existing ion exosphere models. Equations (1) and (2) are quite limiting, however, and many geophysical processes perturb the potential energy distribution into violation of (1) or (2), causing the calculation to be invalid.

In this study we present a general solution to the Vlasov equation for a free-flowing plasma along a magnetic field line using Liouville's theorem, allowing for an arbitrary potential structure including nonmonotonicities. We will first explore the constraints of the existing collisionless kinetic transport models, describe the need for a more general approach to the problem of self-consistent potential energy calculations, and then discuss a technique that handles an arbitrary potential energy distribution along the field line. Finally, the implementation of this model for ionospheric outflows and magnetospheric precipitation will be examined and described, including self-consistent results for the polar wind, along with some of the possibilities for this model.

2. Calculations in E-μ Space

The quantities of interest for each plasma population are the density (for use in the quasineutrality calculation), the field-aligned flux (for use in the current balance condition), the pressure (for determining the local plasma temperature), and

the energy flux. These quantities are calculated as follows [e.g., *Lemaire and Scherer*, 1971]:

$$n = \iiint_{\infty} f(\vec{v}) d^3v \tag{3a}$$

$$\phi = nu = \iiint_{\infty} v_{||} f(\vec{v}) d^3v \tag{3b}$$

$$P_{||} = m \iiint_{\infty} v_{||}^2 f(\vec{v}) d^3v \tag{3c}$$

$$P_{\perp} = \frac{m}{2} \iiint_{\infty} v_{\perp}^2 f(\vec{v}) d^3v \tag{3d}$$

$$\varepsilon_{||} = \frac{m}{2} \iiint_{\infty} v^2 v_{||} f(\vec{v}) d^3v \tag{3e}$$

Note that (3c)-(3e) are total pressure and energy flux, and in order to obtain the temperatures or heat flux, the advective part must be subtracted out.

As particles move along the field line, their velocity vector will change direction and magnitude due to changes in the potential energy or magnetic field. This creates forbidden regions in velocity space that are inaccessible due to the collisionless nature of the calculation. *Lemaire and Scherer* [1970] presented a concise description of the problem in $v_{||}$-$v_{\perp}$ space, complete with a description of the various populations and their regions of existence in velocity space. Performing the calculation in these variables, however, requires the distribution function f used in the integrations to vary along the field line and a careful description of the boundaries separating these populations. Later, *Whipple* [1977] presented the problem in terms of the total energy E and the first adiabatic invariant μ, which are both constants of motion in a collisionless plasma. This relieved the need for changing f along the field line, but boundary descriptions still had to be carefully assigned. It is this E-μ formulation that will be used throughout this study.

The total energy E of a plasma particle is the sum of its kinetic (W) and potential (Π) energies,

$$E = W_{||} + W_{\perp} + \Pi = \frac{mv_{||}^2}{2} + \frac{mv_{\perp}^2}{2} + \Pi \tag{4}$$

and the first adiabatic invariant μ is given by

$$\mu = \frac{W_{\perp}}{B} = \frac{mv_{\perp}^2}{2B} \tag{5}$$

where B is the geomagnetic field strength. The definitions in (3) can be converted into these new variables, with the integrals transformed using $dv_x dv_y dv_z = \Im dE d\mu d\varphi$, where the Jacobian is

$$\Im = \frac{B}{\sqrt{2m^3(E - \mu B - \Pi)}}$$

Note that the use of μ implies a guiding center approximation, and the validity of this assumption will be discussed in the conclusions. When averaged over a gyration of the particle about the magnetic field line, (3) has the form

$$n = \frac{\sqrt{2}\pi B}{m^{3/2}} \iint \frac{f(E,\mu)}{\sqrt{E - \mu B - \Pi}} dE d\mu \tag{6a}$$

$$\phi = \frac{2\pi B}{m^2} \iint f(E,\mu) dE d\mu \tag{6b}$$

$$P_{||} = \left(\frac{2}{m}\right)^{3/2} \pi B \iint \sqrt{E - \mu B - \Pi} f(E,\mu) dE d\mu \tag{6c}$$

$$P_{\perp} = \frac{\sqrt{2}\pi B^2}{m^{3/2}} \iint \frac{\mu f(E,\mu)}{\sqrt{E - \mu B - \Pi}} dE d\mu \tag{6d}$$

$$\varepsilon_{||} = \frac{2\pi B}{m^2} \iint (E - \Pi) f(E,\mu) dE d\mu \tag{6e}$$

It should be noted that Π is an arbitrary potential energy structure and can include an electrostatic potential energy of the form $\pm e\varphi$, a gravitational potential energy of the form $m\Psi_g$, or other potential energies, such as those from spatially integrating the ponderomotive or centrifugal forces (see Appendix A). The mass and charge dependencies can make Π different for each plasma species.

The conversion of the distribution function from Cartesian velocity space to these new variables is quite beneficial because the replacement of the velocity components also acts to remove the spatial dependence in f. That is, f is no longer a function of the potential energy and magnetic field at point s, only the potential energy and magnetic field at the reference altitude s_o. This is because the new velocity variables are constants of motion in a collisionless plasma. Of course, the distribution function in E-μ space, $\phi(E,\mu)$, depends on the potential energy and magnetic field due to to the transformation Jacobian ($\phi = 2Wf/m^2$), and the filled region of E-μ space (i.e., the region of integration) also depends on Π and B.

The function $f(E,\mu)$ is then defined at the reference altitude and can be mapped to any point along the field line. The problem which should be solved is the calculation of the region of the E-μ plane filled by particles for an arbitrary point along the field line. For a given plasma in a given magnetic field, this region is determined by the location of the source of the particles (reference point s_o on the magnetic field line) and by the conservation laws (4) and (5),

$$v_{||}^2 \geq 0; \qquad E - \mu B - \Pi \geq 0 \tag{7}$$

We will restrict our analysis to the case of a one-to-one relation between distance and field strength, i. e., the magnetic field is a monotonic function of s. The possible filled regions can be constructed from a few elementary regions, discussed in Appendix B. However, the new variables obscure the hemispherical direction of the distribution function because of squaring of $v_{||}$ in (4). The two hemispheres of velocity space ($v_{||}>0$ and $v_{||}<0$) must be separately defined by letting $f=f^+$ for one hemisphere and f^- for the other. The sign of $v_{||}$ must then be included in (6) from the original definition in (3), such that they are added in the density and pressure calculations but subtracted in the flux calculations.

Figure 1 shows the filled regions for decelerated (Figure 1a) and accelerated (Figure 1b) particles when the reference point s_o is located at $B=B_{min}$. At s_o the distribution is known, and the function f is defined in the E-μ plane. This means that above the s_o $v_{||}=0$ line defined in (7), f is a given function, say a Maxwellian or bi-Maxwellian, and below this line it is zero.

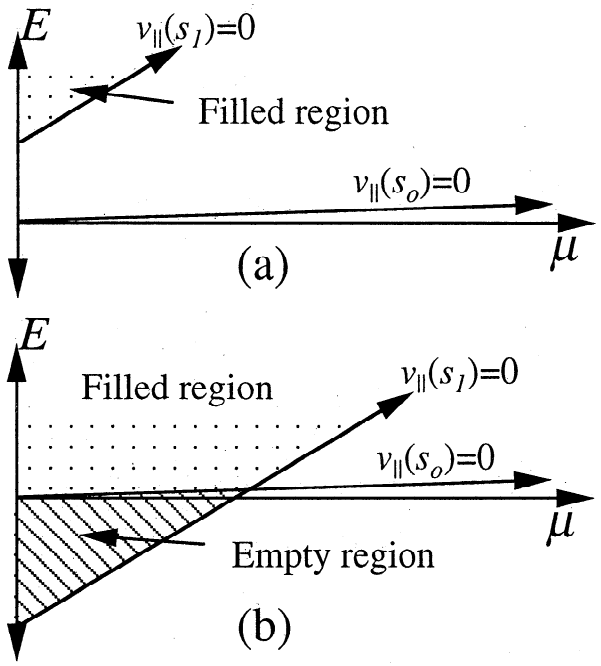

Figure 1. Filled regions in E-μ space for (a) decelerated and (b) accelerated particles at s_1 for the inner magnetosphere case with the reference point at the magnetic equator. The dotted areas are the filled regions, and the striped areas are empty regions in velocity space at s_1. The distribution function f is defined above the s_o $v_{||}$=0 line, with no particles below it.

While the filled region for the decelerated species is defined simply by the $v_{||}$=0 line for the local spatial point s_1, the accelerated species requires two lines to define the region. The space below the s_o $v_{||}$=0 line and above the s_1 $v_{||}$=0 line is an empty region in E-μ space at s_1, created by the acceleration from the potential drop the particles have experienced. The region above the s_o line yet below the s_1 line are particles that have magnetically mirrored between s_o and s_1. For an anisotropic trapped plasma in the magnetosphere, such as that used by *Chiu and Schulz* [1978], this situation corresponds to s_o at the equatorial plane with the decelerated species being the ions and the accelerated species being the anisotropic electrons. The anisotropy will cause the electrons to mirror closer to the equator, and an electric potential develops to maintain charge neutrality.

For a population outflowing from the ionosphere, the reference altitude would be the footprint of the field line, usually somewhere in the topside ionosphere. This point would have the strongest magnetic field rather than the weakest, and so the $v_{||}$=0 lines will start steep and become flatter as B decreases with altitude. The initial distribution function is then defined only in this narrow wedge of E-μ space, and a decelerated species (usually the outflowing electrons) will have some of these particles reflected by the potential barrier.

3. Necessity of a Generalized Model

The filled region, however, is not always as simple as the region above the $v_{||}$=0 lines from (7) for the reference point and the local point. In fact, it is more complicated than this when (1) and (2) are violated. These constraints were originally obtained for Π=-$e\varphi$, and a generalization of these constraints can be summarized as follows (see Appendix B): (1) $d\Pi/dB$ must be monotonic and (2) $d^2\Pi/dB^2>0$ if $d\Pi/dB<0$. These constraints must be satisfied for every population in the calculation throughout the entire spatial domain.

Note that the constraints are on the derivative of the potential energy with respect to the magnetic field strength, not distance. The relationship between distance and magnetic field is shown in Figure 2 for a typical high-latitude field line and an inner magnetospheric field line (equatorial plane geocentric distance of 4 R_E, L=4). In the following discussion, note that the reference point for ionospheric outflows is the ionospheric boundary, while the reference point for trapped and precipitating populations is the magnetospheric boundary.

3.1. Violation of $d\Pi/dB$ Monotonicity

Let us begin with the requirement of monotonicity for the first derivative of the potential energy with respect to the magnetic field. Consider, for example, oxygen ions outflowing from the polar cap ionosphere. The ambipolar electric force is usually less than the gravitational force on these particles, causing them to decelerate as they flow up the field line. For a moderate ambipolar field, this situation will generate a total potential energy distribution that satisfies the generalization of (1) and (2). However, if superthermal electrons dominate at high altitudes, the ambipolar force can surpass gravity, causing the total potential to decrease with altitude. Calculations based on the generalized model of section 4 indicate that photoelectron concentrations of 0.03% can cause the O^+ ions to violate this criterion [*Liemohn et al.*, 1997b]. Other forces could also cause this kind of change in the slope, such as centrifugal acceleration due to convection of the field line across the polar cap or ponderomotive force effects from low-frequency waves. These effects increase with altitude [*Li and Temerin*, 1993; *Horwitz et al.*, 1994] and quite easily surpass the gravitational effects, even for modest convection and wave strengths. Figure 3 shows a calculation of the total potential for O^+ with the ponderomotive (PM) or centrifugal (C) force added in for various electric field strengths (perpendicular wave electric field of 10-150 mV/m for Ψ_{PM} and convection electric fields of 10-100 mV/m for Ψ_C at 500 km). Here the total potential energy Π is calculated using the electrostatic and gravitational potential energies from results from *Khazanov et al.* [1997] with the inclusion of either $m\Psi_{PM}$ from (A4) for the ponderomotive potential energy (Figure 3a) or $m\Psi_C$ from (A8) for the centrifugal potential energy (Figure 3b). Because Ψ_{PM} includes the mass density of the plasma, a

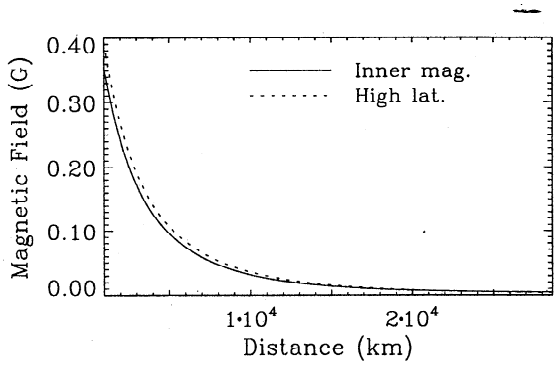

Figure 2. Geomagnetic field strength as a function of distance for a high-latitude field line (solid curve) and an L=4 inner magnetospheric field line (dotted curve).

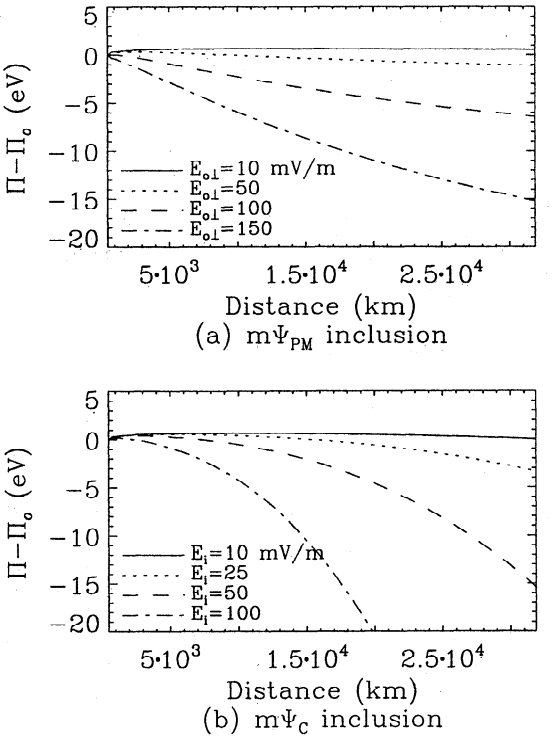

Figure 3. Total potential energies from *Khazanov et al.* [1997] with the inclusion of (a) ponderomotive force potential energies for the given wave electric fields and (b) centrifugal force potential energies for the given convection electric fields.

rigorous calculation of this potential energy should be done only self-consistently, but this plot still shows the dominant influence of these potential energies, even for moderate electric fields.

Violation of the monotonicity of the first derivative for the case of ionospheric outflow is illustrated in Figure 4, showing the total potential energy difference for a decelerated species as a function of distance and magnetic field in Figures 4a and 4b, respectively. The potential is defined so $\Pi(s_\infty)=0$. The point s_1 is at the maximum of the potential energy barrier, and s_2 is somewhere beyond this barrier. Figure 4c shows the filled region in E-μ space for the point s_2. Remember that the distribution function is nonzero above the s_0 $v_{||}=0$ line, and everything to the right and below this line is defined as empty. So while the permitted region at s_2 is above the s_2 $v_{||}=0$ line, the distribution function is zero for part of this region (the striped region in Figure 4c). This empty region represents a source cone distribution where velocity space beyond the pitch angles that map to the ionosphere are empty. Because of the potential energy barrier maximum at s_1, though, all of the particles below the s_1 $v_{||}=0$ line have been reflected, and thus the region between the s_1 and s_2 lines is also an empty region in the distribution function at s_2. This new empty region is caused by the acceleration of the particles due to the potential drop from s_1 to s_2, and the potential energy distribution no longer satisfies the conditions for validity of the previous models.

This violation of monotonicity can occur similarly for the inner magnetospheric case. This situation can occur if some other process besides the electric field dominates the potential structure near the ionosphere, perhaps gravity. If a change in the slope of Π occurs in this case, a change in the filled region for the decelerated particles will occur, shown in Figure 5. Before s_1, the filled region is simply the area above the $v_{||}=0$ line for that altitude because the particles are decelerated by the potential energy difference and reflected by the increasing magnetic field. At some s_2 beyond s_1, however, an empty region now appears near $v=0$ as they are accelerated through the potential energy drop. Note that there was no empty region for the decelerated species for the previous models because the s_2 line is completely above the s_0 line.

3.2. Violation of $d^2\Pi/dB^2>0$ If $d\Pi/dB<0$

A more frequent violation of the constraints is the violation of the one on the second derivative. For high-latitude regions, this can occur quite easily for the decelerated species if the dominant ion changes from oxygen to hydrogen somewhere along the field line. This causes a change in the ambipolar electric field, so the total potential energy will have two characteristic slopes with a knee at the changeover (Figure 6a).

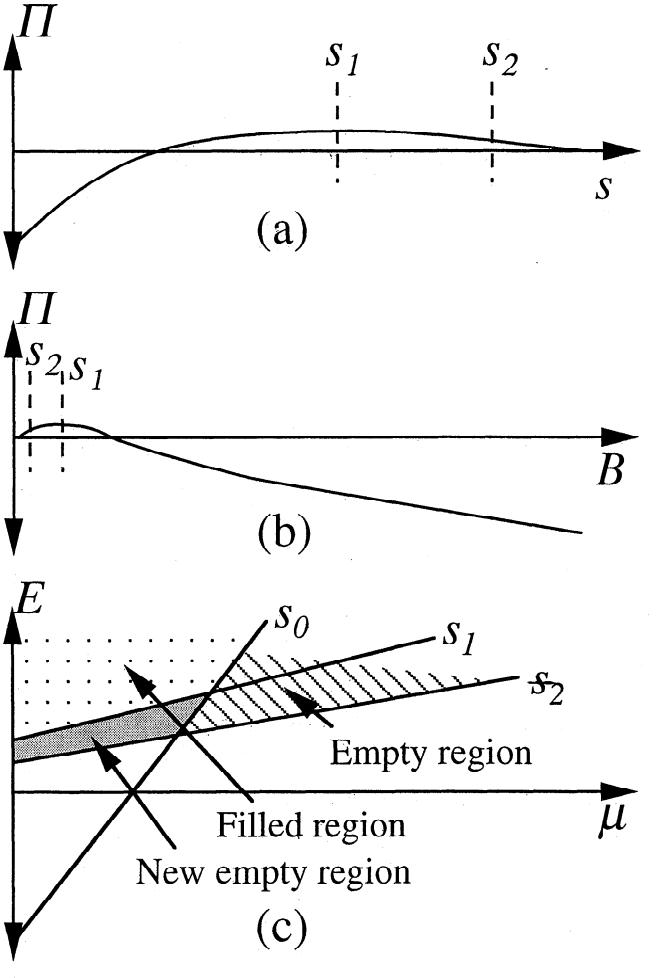

Figure 4. The violation of $d\Pi/dB$ monotonicity along a high-latitude field line for outflowing decelerated particles, showing (a) Π versus s, (b) Π versus B, and (c) E-μ space showing the filled region (dotted area), the empty region included in the previous models (striped area), and the new empty region (shaded area) at spatial point s_2.

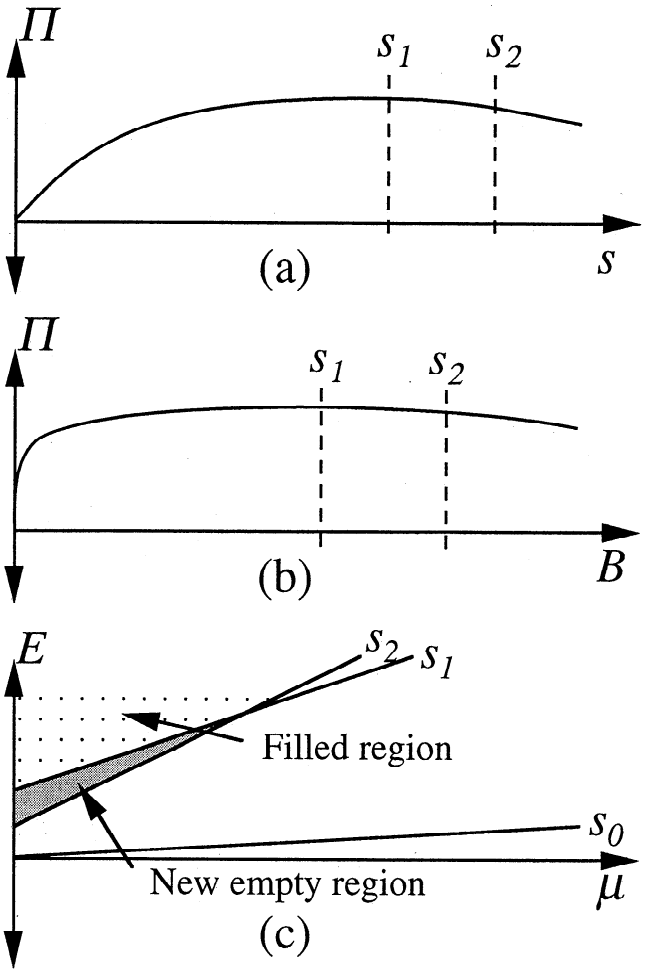

Figure 5. The violation of $d\Pi/dB$ monotonicity along an inner magnetospheric field line for decelerated particles. Plots and shading are the same as in Figure 4.

Calculation of the second derivative with distance from Figure 6a is monotonic. However, the second derivative with respect to B is not (Figure 6b); the knee in Figure 6a transforms into two inflection points in Figure 6b. When this occurs, the integrations in E-μ space at some s_2 between these inflection points will resemble that shown in Figure 6c. As in Figure 4c, the possible region of integration is above the s_2 $v_{||}$=0 line, but the ionospheric source limits the distribution function to a field-aligned cone, creating an empty region (striped area). Because B is now changing faster than Π, a new empty region is also created (shaded area). The particles in this part of E-μ space have been repelled below s_1 and therefore should not be included in the moment calculation at s_2.

The situation can also arise for the hot plasma of the inner magnetosphere. If a process near the ionosphere causes the potential energy distribution to have two characteristic slopes with respect to s, and the knee is near the ionosphere (as shown in Figure 7a), then Π versus B for the accelerated electrons will have two inflection points and the monotonicity of the second derivative will be violated (as seen in Figure 7b). Figure 7c shows the various regions in E-μ space at point s_2. The drop in the potential energy is greater than the increase in the magnetic field, and the intersections of the $v_{||}$=0 lines for s_2 and s_1 with the s_o line are no longer moving monotonically to the left, creating a new empty region (shaded area) between the s_2 and s_1 lines. The striped region is the low-energy hole in the distribution function at s_2 created by the potential energy drop from s_o to s_2.

If $d^2\Pi/dB^2<0$ and $d\Pi/dB<0$ for the entire field line, then every single spatial point from the reference altitude to the endpoint will introduce a new line segment to the definition of the filled region from that point on. In the limit of infinite spatial points these new line segments will form a smooth curve. Figure 8a shows this case for a decelerated population in the ionospheric outflow scenario, and Figure 8b shows it for an accelerated population in the trapped plasma scenario. Although some of the new empty regions in E-μ space can be quite small, their proximity to the low-energy range means that they could cause a significant change in the moment calculations, especially the density calculation.

4. The Generalized Model

It is clear that situations can arise that violate the generalizations of (1) and (2), and the filled region in E-μ space requires more than just the $v_{||}$=0 line defined in (7) for the reference point and the local spatial point. Deriving the moments for each possible scenario would be cumbersome, especially in the final case described in section 3.2. What is needed is a

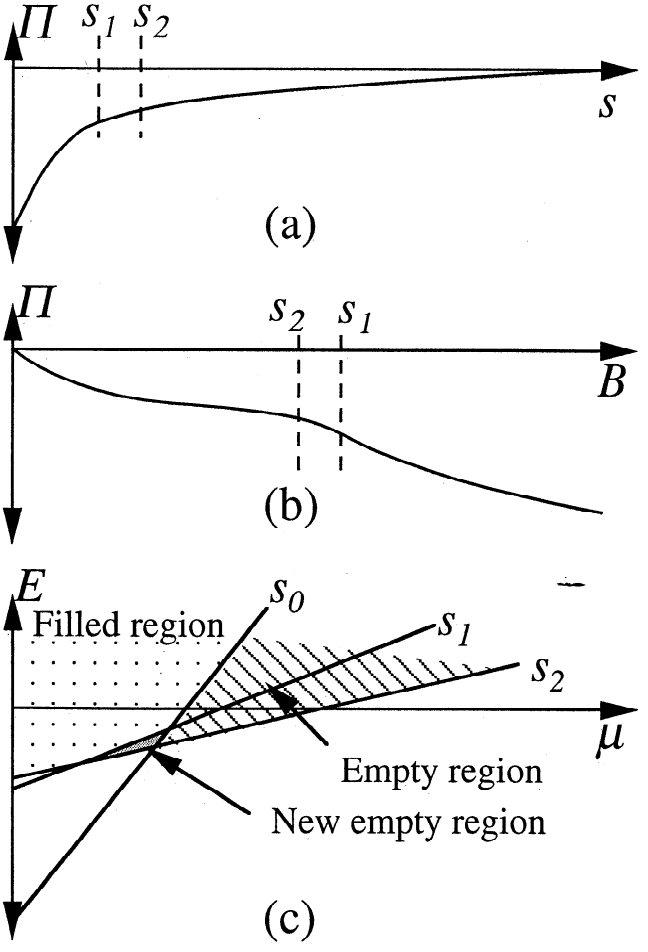

Figure 6. The violation of $d^2\Pi/dB^2$ monotonicity along a high-latitude field line for outflowing accelerated particles. Plots and shading are the same as in Figure 4.

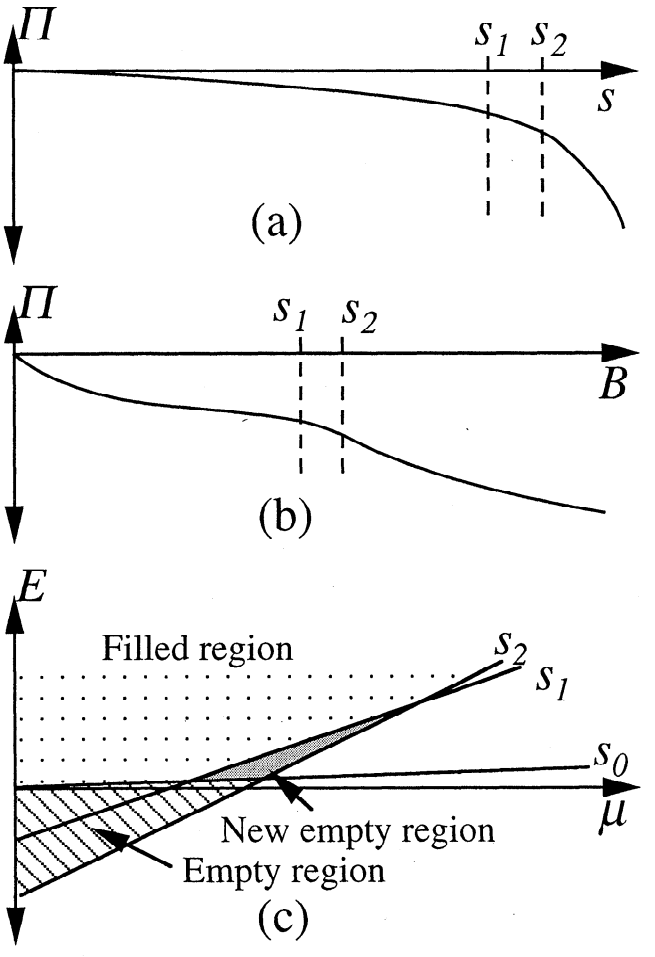

Figure 7. The violation of $d^2\Pi/dB^2$ monotonicity along an inner magnetospheric field line for accelerated particles. Plots and shading are the same as in Figure 4.

general formulation applicable for any number of lines defining the filled region at any spatial point along the field line.

This can be achieved by solving the problem for the dotted region in Figure 9. It defines a region of E-μ space above an arbitrary $v_{||}$=0 linc between two arbitrary μ endpoints. Integration over this area at some spatial point s represents an arbitrary integral of the type needed to address this problem. This yields the general integral

$$I_j(B_\alpha,\Pi_\alpha,\mu_1,\mu_2)=\int_{\mu_1}^{\mu_2}\left[\int_{\mu B_\alpha+\Pi_\alpha}^{\infty}F_j(E,\mu)dE\right]d\mu \tag{8}$$

where F_j is the appropriate kernel from the definition in (6), with B=B_s and Π=Π_s. In (8), B_α, Π_α, μ_1, and μ_2 do not need to be specifically defined to perform this integral but will eventually be defined by a length of some $v_{||}$=0 line it is necessary to integrate above. With this definition, the solution over this arbitrary region of E-μ space is what we need for a generalization of the previous models. From this we can put together a summation of these integrals to obtain the needed moments of the distribution function.

4.1. The Bi-Maxwellian Distribution Function

It is now necessary to define the distribution function at the reference altitude. While the use of any function is possible, a bi-Maxwellian distribution will be used here. This derivation is outlined in Appendix C, and the final solution for a bi-Maxwellian is as follows:

$$n_{\rm gen}=\frac{n_o}{2}\frac{A_1}{1+A\frac{B_o}{B_s}}e^{\frac{\Pi_o-\Pi_s}{T_{||}}}\left\{\mathrm{erfc}\left(\sqrt{x_1}\right)\exp\left(-\frac{\mu_1(B_s+AB_o)}{T_{||}}\right)-\mathrm{erfc}\left(\sqrt{x_2}\right)\exp\left(-\frac{\mu_2(B_s+AB_o)}{T_{||}}\right)+G_1(y)exp\left(\frac{B_s+AB_o}{B_\alpha-B_s}\frac{\Pi_\alpha-\Pi_s}{T_{||}}\right)\right\} \tag{9a}$$

$$\phi_{\rm gen}=\frac{n_o}{2}\sqrt{\frac{2T_{||}}{\pi m}}\frac{B_s}{B_\alpha}\frac{A_1}{1+\frac{B_o}{B_\alpha}A}e^{\frac{\Pi_o-\Pi_\alpha}{T_{||}}}\times\left[\exp\left(-\frac{\mu_1(B_\alpha+AB_o)}{T_{||}}\right)-\exp\left(-\frac{\mu_2(B_\alpha+AB_o)}{T_{||}}\right)\right] \tag{9b}$$

$$P_{||,\rm gen}=n_{\rm gen}T_{||}+\tfrac{1}{2}n_oT_{||}\frac{A_1}{1+A\frac{B_o}{B_s}}G_3(y)\times\exp\left(\frac{\Pi_o-\Pi_s}{T_{||}}+\frac{B_s+AB_o}{B_\alpha-B_s}\frac{\Pi_\alpha-\Pi_s}{T_{||}}\right) \tag{9c}$$

$$P_{\perp,\rm gen}=\frac{P_{||,\rm gen}}{1+A\frac{B_o}{B_s}}+\frac{n_oT_{||}}{2}e^{\frac{\Pi_o-\Pi_s}{T}}\frac{A_1}{\left(1+A\frac{B_o}{B_s}\right)^2}\times\left\{\frac{\mu_1(B_s+AB_o)}{T_{||}}\mathrm{erfc}\left(\sqrt{x_1}\right)\exp\left(-\frac{\mu_1(B_s+AB_o)}{T_{||}}\right)-\frac{\mu_2(B_s+AB_o)}{T_{||}}\mathrm{erfc}\left(\sqrt{x_2}\right)\exp\left(-\frac{\mu_2(B_s+AB_o)}{T_{||}}\right)+\frac{\Pi_\alpha-\Pi_s}{T_{||}}G_2(y)\exp\left(\frac{B_s+AB_o}{B_\alpha-B_s}\frac{\Pi_\alpha-\Pi_s}{T_{||}}\right)\right\} \tag{9d}$$

$$\varepsilon_{||,\rm gen}=\left(\Pi_\alpha-\Pi_s+T_{||}\left[1+\left(\frac{B_\alpha}{B_\alpha+B_oA}\right)^2\right]\right)\phi_{\rm gen}+\frac{n_o}{2}\sqrt{\frac{2T_{||}}{\pi m}}e^{\frac{\Pi_o-\Pi_\alpha}{T_{||}}}\frac{B_sA_1B_\alpha}{B_\alpha+B_oA}\left[\mu_1\exp\left(-\frac{\mu_1(B_\alpha+B_oA)}{T_{||}}\right)-\mu_2\exp\left(-\frac{\mu_2(B_\alpha+B_oA)}{T_{||}}\right)\right] \tag{9e}$$

where x, y, A_1, and A are

$$x_{1,2}=\frac{\mu_{1,2}(B_\alpha-B_s)+\Pi_\alpha-\Pi_s}{T_{||}}$$
$$y=\frac{B_\alpha+AB_o}{B_\alpha-B_s}\qquad A_1=A+1=\frac{T_{||}}{T_\perp} \tag{10}$$

and the three G functions are defined as

$$G_1(y)=\begin{cases} y=0: & G_1=\dfrac{2}{\sqrt{\pi}}\left[\sqrt{x_1}-\sqrt{x_2}\right] \\ y>0: & G_1=\dfrac{1}{\sqrt{y}}\left[\operatorname{erf}\left(\sqrt{yx_1}\right)-\operatorname{erf}\left(\sqrt{yx_2}\right)\right] \\ y<0: & G_1=\dfrac{2}{\sqrt{-y\pi}}\left[e^{-yx_1}D\left(\sqrt{-yx_1}\right)-e^{-yx_2}D\left(\sqrt{-yx_2}\right)\right] \\ y\to\infty: & G_1=0 \end{cases} \tag{11a}$$

$$G_2(y)=\begin{cases} y=0: & G_2=\dfrac{2y}{\sqrt{\pi}}\left(\dfrac{B_s+AB_o}{B_\alpha+AB_o}\right)\left[\sqrt{x_1}-\sqrt{x_2}\right] \\ y>0: & G_2=\sqrt{y}\left(\dfrac{B_s+AB_o}{B_\alpha+AB_o}\right)\left[\operatorname{erf}\left(\sqrt{yx_1}\right)-\operatorname{erf}\left(\sqrt{yx_2}\right)\right] \\ y<0: & G_2=-2\sqrt{\dfrac{-y}{\pi}}\left(\dfrac{B_s+AB_o}{B_\alpha+AB_o}\right)\times\left[e^{-yx_1}D\left(\sqrt{-yx_1}\right)-e^{-yx_2}D\left(\sqrt{-yx_2}\right)\right] \\ y\to\infty: & G_2=0 \end{cases} \tag{11b}$$

$$G_3(y)=\begin{cases} y=0: & G_3=\dfrac{2y}{3\sqrt{\pi}}\left(\dfrac{B_s+AB_o}{B_\alpha+AB_o}\right)\left[x_1^{3/2}-x_2^{3/2}\right] \\ y>0: & G_3=\left(\dfrac{B_s+AB_o}{B_\alpha+AB_o}\right)\left[\dfrac{\operatorname{erf}\left(\sqrt{yx_1}\right)}{\sqrt{y}}-\sqrt{\dfrac{x_1}{\pi}}e^{-yx_1}-\dfrac{\operatorname{erf}\left(\sqrt{yx_2}\right)}{\sqrt{y}}+\sqrt{\dfrac{x_2}{\pi}}e^{-yx_2}\right] \\ y<0: & G_3=\dfrac{1}{\sqrt{\pi}}\left(\dfrac{B_s+AB_o}{B_\alpha+AB_o}\right)\left[e^{-yx_1}\times\left(\dfrac{D\left(\sqrt{-yx_1}\right)}{\sqrt{-y}}-\sqrt{x_1}\right)-e^{-yx_2}\times\left(\dfrac{D\left(\sqrt{-yx_2}\right)}{\sqrt{-y}}-\sqrt{x_2}\right)\right] \\ y\to\infty: & G_3=0 \end{cases} \tag{11c}$$

The solution for an isotropic Maxwellian distribution at the reference point is obtained by setting $T_{||}=T_\perp$, thus setting $A=0$.

4.2. Other Distribution Functions

Results for other distribution functions can also be obtained. The application of the current-potential energy relationship was chosen for this comparison. Finding the relation between the current density and the field-aligned potential has long been a topic of critical importance. *Knight* [1973] was one of the first to consider the self-consistent formation of a field-aligned potential drop due to field-aligned currents,

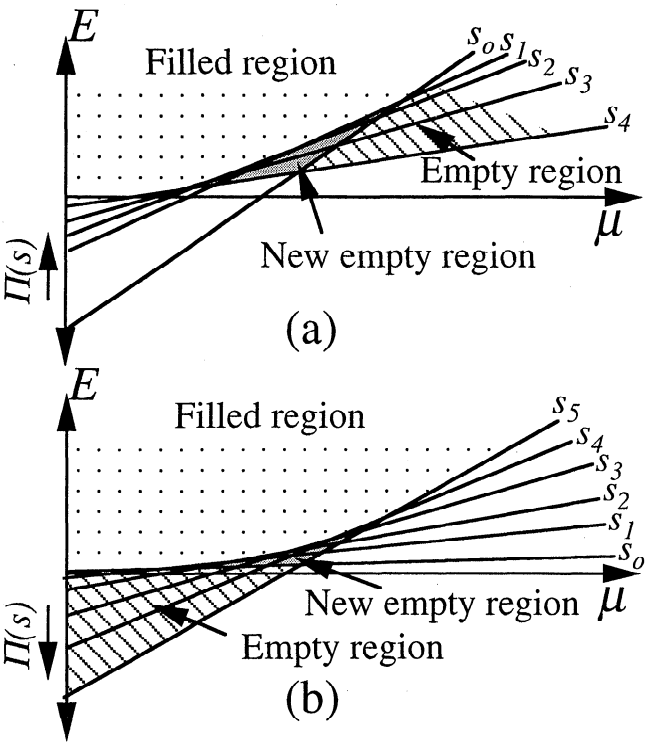

Figure 8. Violation of the sign difference for the first and second derivatives of Π with respect to B for (a) a high-latitude field line for a decelerated species, and (b) an inner magnetospheric field line for an accelerated species. Definitions of the shading are the same as in Figure 4. Note that each spatial point will insert another line into the definition of the filled region all the way to s_∞.

and a good discussion of this topic is presented by *Lyons and Williams* [1984]. From the present model, applying various distribution functions for the particle flux calculation along the field line will yield a general relation for the current density as a function of the field-aligned potential energy.

The method is analogous to that shown in Appendix C, except that the bi-Maxwellian is replaced with a different function, such as a bi-Lorentzian,

$$f=\left(\frac{m}{2\pi}\right)^{3/2}\frac{n_oA_1}{\tau_{||}^{3/2}}\left(\frac{\mu B_oA_1}{\tau_{||}}\right)^{\sigma}\frac{\xi_\kappa^0}{\kappa^{3/2}}\times\left(1+\frac{E-\Pi_o+\mu B_oA}{\kappa\tau_{||}}\right)^{-(\kappa+1)} \tag{12}$$

This is quite general and can be reduced to many other useful distribution functions. In (12), κ defines the slope of the high-energy tail; $\tau_{||}=T_{||}(\kappa-3/2)/\kappa$; $\xi_\kappa^0=\Gamma(\kappa+1)/\Gamma(\kappa-1/2)$; and Γ is the gamma function. Here are the flux integrals, which are easily related to the current density, for a bi-Lorentzian distribution,

$$\phi_{\text{gen}}^{\text{bi-L}}=\frac{n_o}{2}\sqrt{\frac{2\tau_{||}}{m\pi}}\frac{B}{B_\alpha}\frac{\xi_\kappa^0}{\kappa^{1/2}(\kappa-1)}\frac{A_1}{1+\frac{B_o}{B_\alpha}A}\times\left[\left(1+\frac{\mu_1(B_\alpha+B_oA)-\Pi_o+\Pi_\alpha}{\kappa\tau_{||}}\right)^{-(\kappa-1)}-\left(1+\frac{\mu_2(B_\alpha+B_oA)-\Pi_o+\Pi_\alpha}{\kappa\tau_{||}}\right)^{-(\kappa-1)}\right] \tag{13}$$

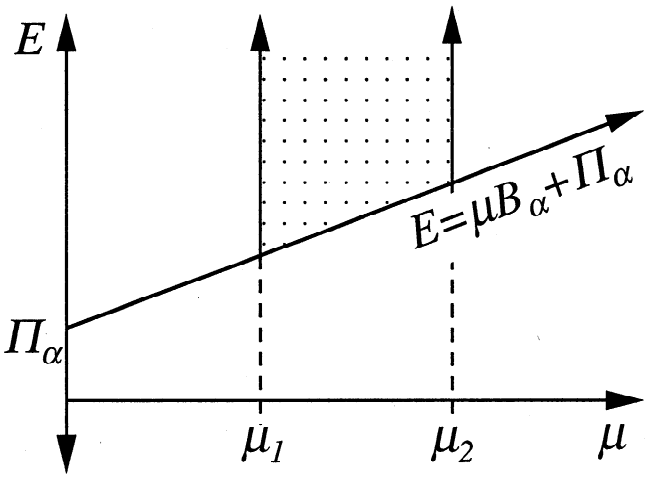

Figure 9. Schematic of an integration over a region of E-μ space (dotted area) above an arbitrary $\nu_{||}$=0 line with arbitrary μ endpoints.

an isotropic Lorentzian distribution,

$$\phi_{\text{gen}}^{\text{L}} = \frac{n_o}{2}\sqrt{\frac{2\tau}{m\pi}}\frac{B}{B_\alpha}\frac{\xi_\kappa^0}{\kappa^{1/2}(\kappa-1)} \times\left[\left(\zeta_1^\alpha\right)^{-(\kappa-1)}-\left(\zeta_2^\alpha\right)^{-(\kappa-1)}\right] \tag{14}$$

and an isotropic Maxwellian distribution,

$$\phi_{\text{gen}}^{\text{M}} = \frac{n_o}{2}\sqrt{\frac{2T}{\pi m}}\frac{B_s}{B_\alpha}e^{\frac{\Pi_o-\Pi_\alpha}{T}}\left[e^{-\frac{\mu_1 B_\alpha}{T}}-e^{-\frac{\mu_2 B_\alpha}{T}}\right] \tag{15}$$

where $\zeta_{1,2}^\alpha = 1+\left(\mu_{1,2}B_\alpha+\Pi_\alpha-\Pi_o\right)/\kappa\tau$. The derivation of the complete set of moments (up to heat flux) for these and other distributions is presented by *Liemohn and Khazanov* [1998].

4.3. Implementation

To obtain the proper piecewise integration for a given spatial location along the field line, it is necessary to know the development of the potential energy structure from the reference altitude up to the desired point. So although this is an analytical solution, a numerical grid in space is needed to define these regions of integration. It also means that these spatial points must be close enough to accurately resolve the correct shape of the filled region for a given spatial point. In the presence of counterstreaming populations (f^+ and f^-), the potential energy structure beyond the desired point will also affect the solution, and an iterative process over the entire spatial range must be performed. If, however, the potential energy solution satisfies the generalized constraints in section 3, then any spatial step is fine because the definition of the filled region reduces to the $\nu_{||}$=0 lines of the local point and the reference point.

For an arbitrary potential energy distribution, the regions of integration can become very complex and a complicated interplay arises between the populations in determining the boundaries in velocity space. It is thus useful to show these boundaries for a case study, and an appropriate choice is when the generalized constraints are met. This situation is complicated enough, and it provides a validation of this formulation compared with that of previous models. This discussion of the velocity space regions for the various populations and a comparison with the model of *Lemaire and Scherer* [1970, 1971, 1972] is given in Appendix D.

5. Applications of the General Formulation

To quantitatively demonstrate the influence of the change in the integration region that this new model specifies, results are shown here for two scenarios: precipitation of a magnetospherically trapped hot population and outflow from the high-latitude ionosphere.

5.1. Precipitation

The quantitative effects of including other nonlocal $\nu_{||}$=0 lines besides that of the reference point can be readily seen by considering magnetospheric precipitation. Magnetospheric precipitation was included in the studies of *Lemaire and Scherer* [1973], *Knight* [1973], *Whipple* [1977], *Chiu and Schulz* [1978], *Stasiewicz* [1985], *Washimi and Katanuma* [1986], *Miller and Khazanov* [1993], and *Wilson et al.* [1997], and the resulting formulas are all very similar in that the density or flux at the ionospheric boundary is determined by the total potential drop and magnetic field change between the spatial domain endpoints.

To demonstrate the importance of the generalized formulation, let us calculate the density and flux of the accelerated electrons reaching the ionospheric boundary using the new formulas for several different potential energy distributions between the two endpoints. Five potential energy structures will be considered here, and they are shown in Figure 10a. All five distributions have the same total potential energy drop of $\Pi/T_{||}$=1, but the shapes are quite different, and so it is expected that the general formulation will calculate different results for each one. A choice of $\Pi/T_{||}$=1 is quite reasonable for magnetospheric precipitation, because the electrostatic potential difference is typically of similar magnitude to the process responsible for its creation, in this case the kinetic energy of the trapped population [*Miller and Khazanov*, 1993]. In Figure 10, curve 1 corresponds to a potential energy that satisfies the generalized constraints, while curves 2-5 violate these constraints in some way. Such total potential energy structures could be created by incorporating the additional potential energy terms discussed in Appendix A. Figures 10b and 10c show the first and second derivative of Π with respect to B. To satisfy the generalized constraints, the corresponding curve in Figure 10b must be monotonic, and if this curve is less than zero, then the corresponding curve in Figure 10c must be greater than zero everywhere. Of the five curves drawn, it is clear that only curve 1 satisfies the criteria.

Each of these curves can be used to obtain a filled region for the precipitating part of a trapped population. For this study, the $\nu_{||}$=0 lines of 500 equidistant spatial points along an L=4 field line were calculated to determine the filled region for integration at the ionospheric endpoint. The magnetic field distribution used is given in Figure 2, and the anisotropy was taken to be A=-0.5 (so from (12), $T_\perp$=2$T_{||}$). The resulting density, flux, and number of integration regions ($\alpha_{\max}$) for curves 1-5 in Figure 10 are presented in Table 1. The bump in curve 2 near the ionosphere caused the density to drop nearly in half, and the smooth curve 4 had nearly every spatial point contributing to its ionospheric integration region. These lines form a hyperbola above the simple two-line region of curve 1.

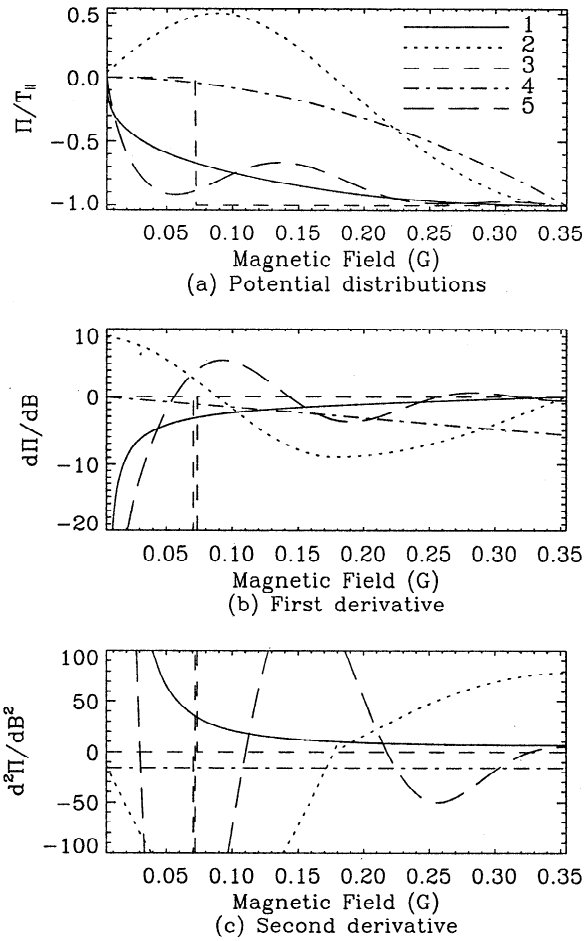

Figure 10. (a) Potential energy distributions for magnetospherically trapped population with a net acceleration toward the ionosphere. All five curves have the same final potential energy drop equal to the population's parallel temperature. Also shown are (b) their first derivatives with respect to the magnetic field B and (c) their second derivatives with respect to B.

The two lines of curve 3 are not the same as the two lines of curve 1; the reference point $v_{\|}$=0 line has been replaced by the line for the spatial point just before the potential drop. Incidentally, curve 5 has exactly the same ionospheric solution as curve 1. This is because all of the violations along the field line happen to be obscured by the ionospheric $v_{\|}$=0 line. However, the moment calculations at most points between the two endpoints will be quite different from those of curve 1, and most of the integration regions for curve 5 at an arbitrary s will have more than two defining lines.

It should be noted that these differences in density and flux are caused by the changes in the integration region due to the various shapes of the field-aligned potential energy structures. All five results have the same total potential energy drop, and so these potential energy distributions would yield identical moment results using the previous models.

5.2. Ionospheric Outflow

The total potential energy drop used in section 5.1 is equal to the parallel temperature of the plasma population. This is reasonable for calculations of trapped hot plasmas because the plasma kinetic energy is the primary generator of the field-aligned potential difference [*Miller and Khazanov*, 1993]. For the case of ionospheric outflows, however, the potential energy difference can be much greater than the plasma temperature because a primary generator of the potential energy difference is gravity. For example, *Khazanov et al.* [1997] calculated a total potential barrier for polar wind oxygen ions ranging from 2 to 6 eV, depending on the photoelectron concentration, while the ion temperature was only 0.17 eV at the reference point. These results were a combination of the graviational potential energy (an 8-eV barrier) and the electrostatic potential energy (a 2- to 6-eV drop). Also, Figure 3 shows that other potential energies can cause the total potential energy difference at high latitudes to be huge compared with the plasma temperature. Therefore a total potential difference of 20 times the plasma temperature will be used for the ionospheric outflow case, which is a conservative estimate of the total potential energy difference experienced by outflowing ions [cf. *Khazanov et al.*, 1997; *Wilson et al.*, 1997]. Two cases will be considered: a net potential energy barrier and a net potential energy drop. Three potential energy distributions along a high-latitude field line are shown in Figure 11a for the case of a net deceleration of the particles. As is seen in Figures 11b and 11c, among the three curves, only curve 6 satisfies the generalized constraints.

To obtain calculations of the escaping particles for this decelerated population, 500 points were used along the high-latitude field line shown in Figure 2 for an isotropic reference altitude distribution (A=0). The resulting density, flux, and number of integration regions (α_{max}) for the curves in Figure 11 are presented in Table 2. It is clear that the potential energy structure as well as the total potential difference are important factors in calculating the moments of the distribution function. Curve 8, while smooth and monotonic, has a hyperbola for a filled region (similar to curve 4 of Figure 10), and its density is almost 4 times less than that of curve 6. Because the particles subjected to curve 7 encountered a maximum barrier of Π/T=25, and those making it past this are then accelerated, this curve yields a density that is over 3 orders of magnitude less than that of curve 6. Note that using the previous models to calculate these moments would yield identical results for curves 6-8.

The case of net acceleration is given in Figure 12, showing three potential energy curves and their first and second derivatives with respect to B. Note that only curve 9 satisfies (8) and (9). A potential energy distribution like curves 9 and 10 would be quite easily created with the inclusion of either the ponderomotive or centrifugal force, as seen Figure 3, and one such as curve 11 is analogous to the potential barrier formation discussed by *Wilson et al.* [1997]. A similar calculation as that for curves 6-8 yields the results shown in Table 3. The density and flux for curve 9 are substantially higher than for

Table 1. Results for Hot Plasma Precipitation

Curve	α_{max}	n/n_o	ϕ/ϕ_o
1	2	.78	1.98
2	28	.40	1.28
3	2	.70	1.87
4	479	.64	1.85
5	2	.78	1.98

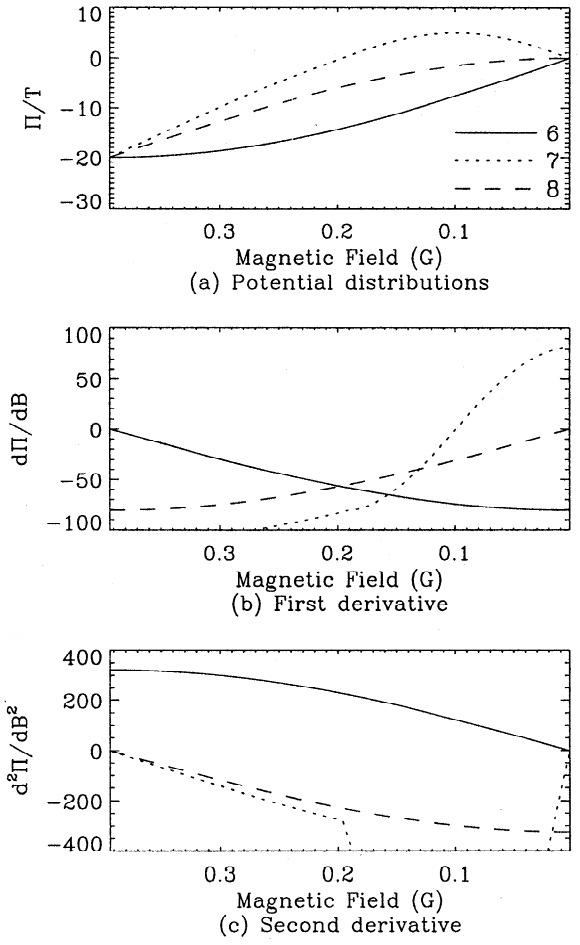

Figure 11. (a) Potential energy distributions for an ionospheric outflow population with a net potential barrier. Also shown are (b) their first derivatives with respect to the magnetic field B and (c) their second derivatives with respect to B.

the other two curves, approaching 2 orders of magnitude difference. The integration region for curve 9 is defined by only one $v_{\|}$=0 line, that at the base of the ionosphere. Note that these densities and fluxes are much higher than the results for curves 6-8 because of the difference in net potential energy.

5.3. Self-Consistent Polar Wind Outflows

A final result to be discussed are initial self-consistent calculations of the new model for polar wind outflow. This will be done by comparing results for this model with similar results from *Khazanov et al.* [1997]. Boundary conditions similar to those described by *Khazanov et al.* [1997] were applied to the new model, including a fluid description for the thermal electrons by solving the momentum and energy equations for the thermal electron density and temperature, respectively, as discussed in that paper. Three levels of n_{p0}, the photoelectron content at the base of the calculation (500 km altitude), are used for these calculations: n_{p0}=0.01%, 0.03%, and 0.05%. These three values were chosen because they represent realistic values of the photoelectron content in the upper ionosphere, as calculated by *Richards et al.* [1994] and *Liemohn and Khazanov* [1995]. A photoelectron concentration of up to 1.0% was used by *Khazanov et al.* [1997] for comparison with the results of *Tam et al.* [1995] and also to show the maximal influence of photoelectrons that should be expected under any conditions in the high-latitude region. An initial guess for the electrostatic potential energy distribution is made, and the model converges to a steady state solution through successive iterations of the field-aligned calculation.

The comparative results between the two models are presented in Figure 13. It can be seen that the total potential energy difference for O^+ changes substantially between the two models for higher levels of n_{p0}. In fact, the result changes from a net deceleration to a net acceleration of O^+. This difference is mainly due to the fact that the new model introduces a hole in the O^+ distribution function at high altitudes, above the altitude of the maximum potential barrier. The previous model filled in this hole, causing the calculation to converge to a different potential energy distribution above this peak barrier. Owing to the dependence of the solution at a given spatial point on those above and below it, the iteration process yields different results for the two models along the entire field line for higher photoelectron concentrations. This change in the potential energy curves has the effect of increasing the density by an order of magnitude in the high-altitude region. Also shown is the thermal electron temperature calculated by the two models. The same energy equation was used in the two models, yet T_e is increased in the new model due to the change in the electrostatic potential energy distribution along the field line. It should be noted that these are preliminary results, and a complete analysis of the effects of the various processes discussed in this paper that could lead to arbitrarily complex potential energy distributions is currently under way.

From these results, it can be stated that the validity of the previous models to the scenario of photoelectron-driven polar wind outflows extends up to moderate but not high photoelectron concentrations. As stated above, 0.05% is a high concentration of photoelectrons in the high-latitude upper ionosphere, but it is clear that the low-energy hole in the O^+ distribution region created by the complexity of the potential energy distribution plays a crucial role in the development of the solution and should be taken into account.

6. Conclusions

The results presented in this study show that the calculation of plasma moments from the Vlasov equation can be much more complicated than originally thought. Common geophysical situations can arise to cause the potential energy distribution along the magnetic field line to violate the generalization of constraints (1) and (2) from *Chiu and Schulz* [1978] (given in section 3 and Appendix B), and that the potential energy distribution along the entire field line must be known (and calculated self-consistently and iteratively) in order to properly obtain the filled regions for the moment calculations at an arbitrary location. In this study, we simplified this prob-

Table 2. Results for Decelerated Polar Wind Outflow

Curve	α_{max}	n/n_o	ϕ/ϕ_o
6	2	2.6×10^{-10}	2.6×10^{-10}
7	304	7.2×10^{-14}	3.3×10^{-13}
8	485	7.2×10^{-11}	1.1×10^{-10}

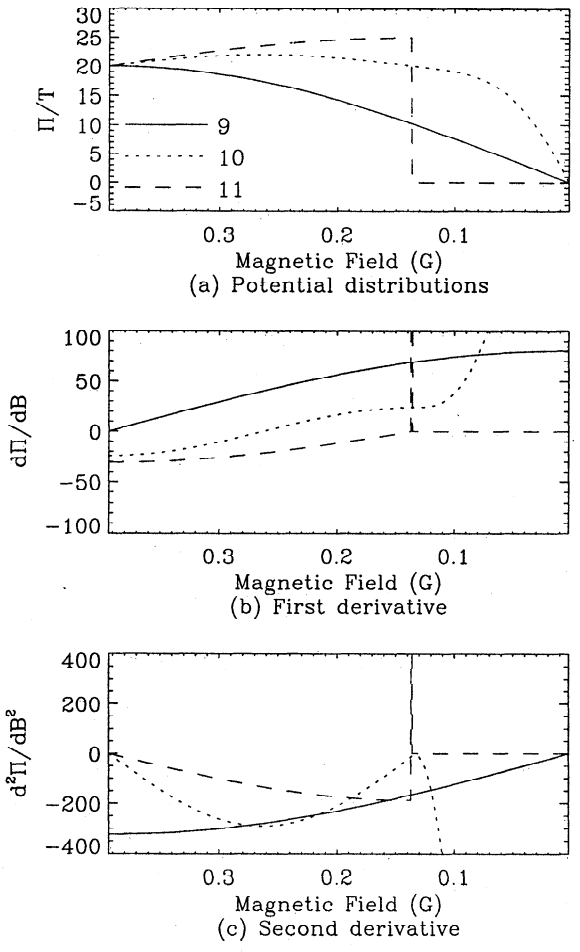

Figure 12. (a) Potential energy distributions for an ionospheric outflow population with a net potential drop. Also shown are (b) their first derivatives with respect to the magnetic field B and (c) their second derivatives with respect to B.

lem in order to clarify some of the issues surrounding this new approach, and thus only initial self-consistent calculations with this new formulation have been shown here.

While the existing models of calculating a self-consistent potential for a collisionless plasma by using Liouville's theorem to solve the Vlasov equation are quite valid and very useful, their validity is limited at least by the generalized constraints on the distribution of the potential with respect to the magnetic field strength. This study presented a generalization to the previous models for the solution of an arbitrary potential energy distribution, including any number of nonmonotonicities. The formulas for a bi-Maxwellian distribution at the reference point are derived and presented in (9). It can handle an arbitrary definition of the reference point, even multiple reference points for different plasma species, and can handle widely varying plasma populations and distribution functions for those populations simultaneously. Also, it can be used for any collisionless plasma situation, where a field-aligned solution is needed. Under similar constraints, this model reduces to the results of previous models.

Using this generalized formulation, it has been shown that the solution can depend on many of the spatial points along the field line (including those above and below the local point), not just the local point and the reference point, and that the solution must be iterated to convergence to insure a result that is consistent between the spatial grid points. For precipitation of magnetospherically trapped hot plasma, this model yields moment calculations that vary by up to a factor of 2. The differences are much greater for the high-latitude outflow scenario, giving order of magnitude variations, depending on the shape of the potential energy distribution between identical total potential differences. A comparison of self-consistent calculations with previous results shows that the low-energy holes in the distribution function discussed in section 3 can dramatically alter the results. Note that a calculation of the characteristic timescale for the plasma to flow through these potential energy differences in these calculations is much longer than their gyroperiod, validating the use of the guiding center approximation (see Appendix E).

The next step for this model is to continue to develop it into a self-consistent calculation for the two situations described in this paper, with the combined effects of the relevant processes. The new formulation has recently been included in the model of *Khazanov et al.* [1997], and initial examination of those and other polar wind results in light of this technique have been presented, showing changes in the total potential energy difference from a net deceleration for O^+ to a net acceleration with a realistic photoelectron concentration at the base. For magnetospheric calculations, the hot plasma is expected to have the most influence on the thermal plasma when the hot particles are enhanced and the low-energy particles are depleted, as is the case during geomagnetically disturbed times [see, for example, *Singh and Horwitz,* 1992; *Birn et al.,* 1997]. A similar numerical model for the hot plasma is also under construction and will be incorporated into the model of *Liemohn et al.* [1997a] to analyze the influences of the hot trapped plasma on plasmaspheric refilling.

Appendix A: Other Possible Potential Energies

A.1. The Ponderomotive Potential of Alfvén Waves

We will follow *Guglielmi et al.* [1996] where the single-particle approach has been used to evaluate the ponderomotive force of an Alfvén wave. Let B be the background magnetic field and $E_\perp$ be the amplitude of the Alfvén wave. Then the field-aligned component of the so-called Miller force in the low-frequency limit $\omega << \Omega_i$ acting on a charged particle with mass m can be presented in the form

$$F_M = \frac{m}{4B^2}\frac{\partial E_\perp^2}{\partial s} \qquad \text{(A1)}$$

where s is geocentric distance and $\partial/\partial s$ is the spatial derivative along the field line. It is useful to note that (A1) can be derived by averaging the Lorentz force over a period of the Alfvén oscillation.

Table 3. Results for Accelerated Polar Wind Outflow

Curve	α_{max}	n/n_o	ϕ/ϕ_o
9	1	7.7×10^{-4}	6.4×10^{-3}
10	109	1.4×10^{-4}	1.2×10^{-3}
11	235	1.1×10^{-5}	1.0×10^{-4}

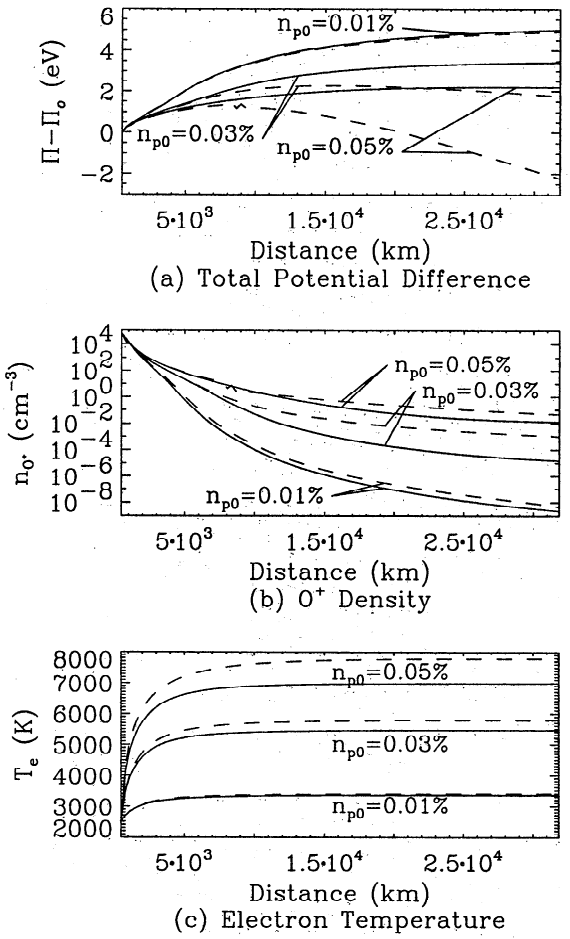

Figure 13. Comparison of the results from *Khazanov et al.* [1997] (solid lines) with those of the new model in the isotropic Maxwellian case (dashed lines). Three values of n_{p0}, the photoelectron content at the base of the run (500 km), are shown along the field line for (a) total potential difference (electrostatic and gravitational) for O^+, (b) O^+ density, and (c) thermal electron temperature.

In addition to (A1), the "magnetic pumping" force

$$F_{LH} = -\frac{m}{2B^2} E_\perp^2 \frac{\partial \ln B}{\partial s} \tag{A2}$$

exists if the background magnetic field is inhomogeneous [*Lundin and Hultqvist*, 1989], which can be rewritten using the well-known relation

$$E_\perp = c_A b \propto B/\rho^{1/4}$$

where $c_A = B/(\mu_o \rho)^{1/2}$ is the Alfvén speed, $\rho = \sum m_\alpha n_\alpha$ is the plasma mass density, b is the magnetic wave amplitude, and μ_0 is the permeability of free space [*Alfvén and Fälthammar*, 1963]. Combining (A1) and (A2), the total ponderomotive force of Alfvén waves $F_{PF} = F_M + F_{LH}$ can be rearranged into the form [*Guglielmi et al.*, 1996]

$$F_{PM} = -m a_{PM} \qquad a_{PM} = (b^2/8\mu_0\rho)\partial \ln \rho/\partial s \tag{A3}$$

Here a_{PF} is the ponderomotive acceleration.

The total ponderomotive force (A3) is independent of B and directed toward decreasing ρ, providing the electromagnetic lift of the background plasma. It is proportional to the mass m and has more influence on the acceleration process of heavy ionospheric ions. Because of the mass density dependence, the ponderomotive force has to be found in the process of the self-consistent coupling of all plasma components based on the quasi-neutrality and currentless conditions.

The ponderomotive potential Ψ_{PM} can be defined as $F_{PM} = -m\nabla\Psi_{PM}$ and presented for our one-spatial-dimension case in the following form:

$$\Psi_{PM} = \frac{2\alpha}{\sqrt{\rho}} \tag{A4}$$

and $\alpha = \sqrt{\rho_0} E_{0\perp}^2/(8B_0^2) = \text{const}$; $E_{0\perp} = E_\perp(s_0)$, $B_0 = B(s_0)$, and $\rho_0 = \rho(s_0)$ are values at a certain point s_0 on a given field line of the geomagnetic field. This s_0 is a reference point where the low-frequency wave amplitude is known or assumed and does not have to be the same reference point as that for the distribution function. Because (A4) contains the mass density, and this moment calculation depends on the potential structure, a self-consistent calculation along the field line should be performed when including this effect.

A.2. Centrifugal Acceleration

In the centrifugal acceleration given by *Horwitz et al.* [1994] for meridional convection across the pole, the approximate parallel acceleration along a polar magnetic field line may be presented in the form

$$a_C^M = 1.5\left(\frac{E_i}{B_i}\right)^2\left(\frac{s^2}{s_i^3}\right) \tag{A5}$$

where E_i, B_i, and s_i refer to the electric and magnetic field magnitudes and geocentric distance along the field line in the ionosphere, respectively. Again, this reference point does not have to be the same reference point as that for the distribution function.

For purely longitudinal convection along a constant L shell the centrifugal acceleration is

$$a_C^L = a_C^M\left(1-\frac{s}{s_i L}\right)^{3/2}\left(1-\frac{3s}{4s_i L}\right)^{5/2} \tag{A6}$$

Similar to the previous subsection, we can also introduce a centrifugal potential Ψ_C

$$F_C = -m\nabla\Psi_C \tag{A7}$$

In the case of meridional convection, this can be presented in the following analytical form in the field-aligned case:

$$\Psi_C^M = -0.5\left(\frac{E_i}{B_i}\right)^2\left(\frac{s}{s_i}\right)^3 \tag{A8}$$

The total potential energy for each plasma component that will be presented in the final expressions for the moments of the distribution function can now be written as

$$\Pi = e_\alpha\varphi - m_\alpha\left(\Psi_G + \Psi_{PM} - \Psi_C\right) \tag{A9}$$

Here φ is self-consistent electrostatic potential; and Ψ_G, Ψ_{PM}, and Ψ_C are gravitational, ponderomotive, and centrifugal potentials, respectively.

Appendix B: Generalization of the *Chiu and Schulz* [1978] Constraints

Because the previous collisionless kinetic models include only the calculation of the local and reference point $v_{||}$=0 lines in their definition of the filled region of velocity space, constraints must be imposed on the the potential energy to insure that the solution is valid. *Chiu and Schulz* [1978] defined these criteria for the electrostatic potential during magnetospheric precipitation, given in (1) and (2). Here these criteria will be extended for an arbitrary potential energy Π. This will be analyzed using three neighboring points: s_{i-1}, s_i, and s_{i+1}, where i is the spatial grid index. The boundary lines for these points are found from (7):

$$E = \mu B_\alpha + \Pi_\alpha; \quad \alpha = i-1, i, i+1 \tag{B1}$$

Let us begin by supposing that s_{i-1} is the reference point and that Π_{i-1}=0, but the argument is easily generalized for any three points in the simulation domain. The region above the line $E = \mu B_{i-1} + \Pi_{i-1}$ is therefore filled at s_{i-1}.

In order for the region of integration to be defined by only the $v_{||}$=0 lines from the reference point and the local point, there is just one necessary and sufficient condition that must be met: If the s_{i+1} $v_{||}$=0 line is ever above the reference point (here s_{i-1}) $v_{||}$=0 line for μ>0, then it must also be above the s_i $v_{||}$=0 line for these μ values. This statement will now be considered, resulting in several constraints on the potential energy distribution.

If the potential energy distribution is nonmonotonic, then this condition will not be met for the decelerated species (see, for example, Figure 1a). Because magnetic field and distance are one-to-one, this requirement can be written as follows: The first derivative of the potential energy with respect to the magnetic field must be monotonic throughout the spatial range.

Beginning with this constraint of monotonicity, a further criterion can be derived by considering the intersection of the $v_{||}$=0 lines. The point of intersection for the lines of spatial points s and $s+ds$ (any two adjacent spatial points) is

$$\mu^* = -\frac{d\Pi}{dB}; \quad E^* = \Pi - B\frac{d\Pi}{dB} \tag{B2}$$

If $d\Pi/dB$>0, μ^* is negative and the lines do not cross in the region of definition (μ>0). This is shown in Figures 14a and 14b for the two cases being discussed (high-latitude outflow

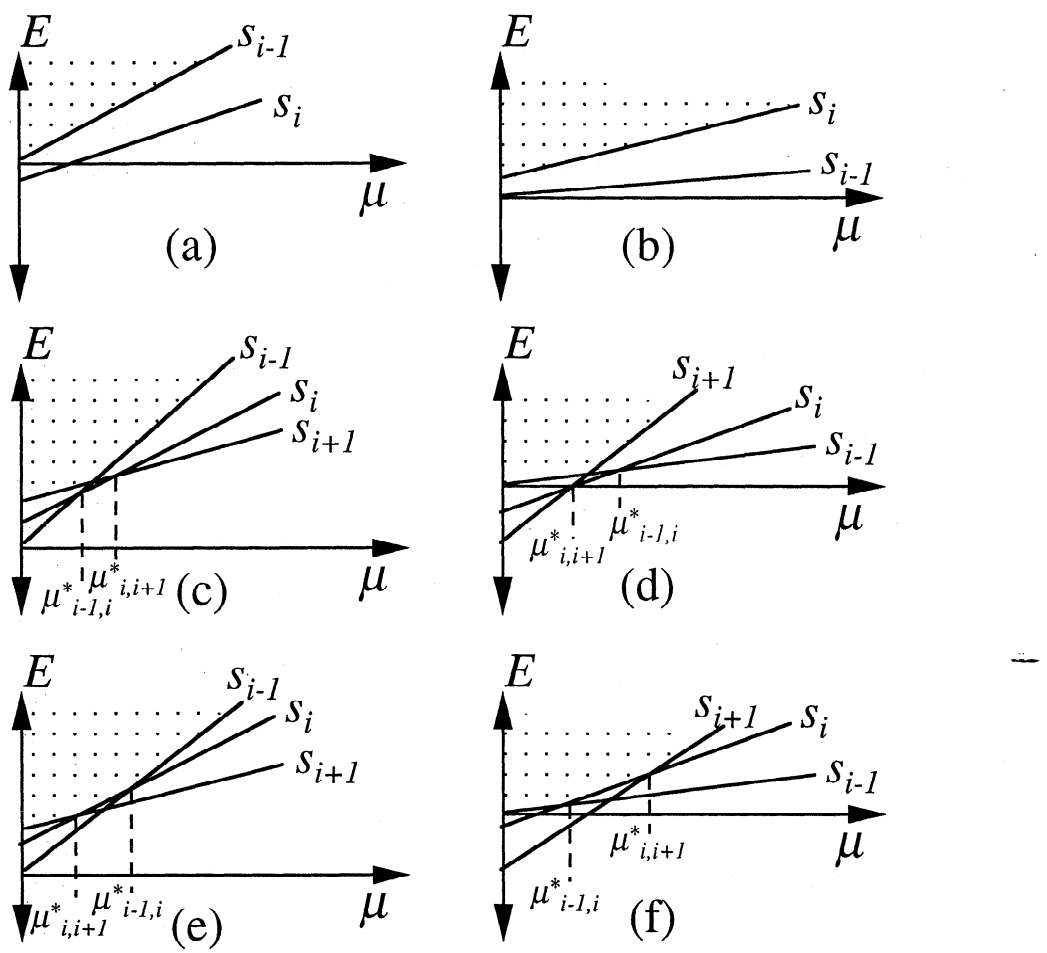

Figure 14. Schematics of the definition of the filled region of velocity space (dotted area) at s_{i+1} based on three neighboring spatial points. The left-hand column is for the ionospheric outflow scenario (dB/ds<0), and the right-hand column is for the magnetospheric trap and precipitation scenario (dB/ds>0). Figures 14a and 14b show the filled region for $d\Pi/dB$>0; Figures 14c and 14d show it for $d\Pi/dB$<0 and $d^2\Pi/dB^2$>0; and Figures 14e and 14f show it for $d\Pi/dB$<0 with $d^2\Pi/dB^2$<0. The top two rows have only two $v_{||}$=0 lines defining the filled region (s_{i-1} and s_{i+1}), while the bottom row shows all three lines participating in the definition (violating the constraints on the previous models).

and the magnetospheric trap). When this derivative is positive, the only criterion on the potential energy for validity of the previous models is monotonicity.

If $d\Pi/dB<0$, then the lines intersect at some $\mu^*>0$. If the points of intersection between lines i-1 and i ($\mu^*_{i-1,i}$) and the intersection between i and $i+1$ ($\mu^*_{i,i+1}$) are arranged so that $\mu^*_{i-1,i}<\mu^*_{i,i+1}$ (i.e., $\mu^*(s)<\mu^*(s+ds)$) and $dB/ds<0$ (outflow case), then $d^2\Pi/dB^2>0$. This sitiuation is shown in Figure 14c, and the filled region is determined by only two lines, from the reference point (i-1) and from the local point (i or $i+1$, but not both). Similarly, if the μ^*s are arranged so that $\mu^*_{i-1,i}>\mu^*_{i,i+1}$ (i.e., $\mu^*(s)>\mu^*(s+ds)$) and $dB/ds>0$ (magnetospheric case), then again $d^2\Pi/dB^2>0$ and the filled region will be determined by the lines from the reference and local points (Figure 14d). Therefore, when the first derivative is monotonically negative and the second derivative is positive, then the previous models will be valid.

Finally, if $d\Pi/dB<0$ and either (a) $\mu^*(s)<\mu^*(s+ds)$ with $dB/ds>0$, or (b) $\mu^*(s)>\mu^*(s+ds)$ with $dB/ds<0$, then the second derivative of Π with respect to B will be negative. When this occurs the boundary of the filled region for point $i+1$ will consist of three line segments. For a situation analogous to that in Figure 14e (outflow), the boundary is defined first by the s_{i+1} line $E=\mu B_{i+1}+\Pi_{i+1}$ up to $\mu^*_{i,i+1}$, then by the s_i line up to $\mu^*_{i-1,i}$, and finally by the ray $E=\mu B_{i-1}+\Pi_{ii-1}$. For Figure 14f (trap), the scenario is similar, but the positions of $\mu^*_{i,i+1}$ and $\mu^*_{i-1,i}$ are reversed. In general, for these cases the filled region of E-μ space depends not only on the reference and local point $v_\parallel=0$ lines but also on the potential energy and magnetic field of other (perhaps all) nonlocal points. Therefore the functional dependence of Π with respect to B, then, that insures the validity of the previous models can be written as two conditions: (1) $d\Pi/dB$ must be monotonic and (2) $d^2\Pi/dB^2$ must be greater than zero if $d\Pi/dB$ is less than zero.

Appendix C: Derivation of the Bi-Maxwellian General Formulation

In Cartesian velocity space, a bi-Maxwellian velocity-space distribution function is given as

$$f=\left(\frac{m}{2\pi}\right)^{3/2}\frac{2n_o}{T_\parallel^{1/2}T_\perp}\exp\left(-\frac{mv_z^2}{2T_\parallel}-\frac{m\left(v_x^2+v_y^2\right)}{2T_\perp}\right) \tag{C1}$$

and, when transformed into our variables, becomes

$$f=\left(\frac{m}{2\pi}\right)^{3/2}\frac{2n_o}{T_\parallel^{1/2}T_\perp}\exp\left(-\frac{E}{T_\parallel}+\frac{\Pi_o}{T_\parallel}-\mu B_o\left[\frac{1}{T_\perp}-\frac{1}{T_\parallel}\right]\right) \tag{C2}$$

in our E-μ coordinate system. Note that $T_\parallel$ and $T_\perp$ are the temperatures at the reference altitude s_o and will not change in the definition of f along the field line.

The moments defined in (6) can now be obtained for the general integral defined in (8) over the arbitrary E-μ space region in Figure 9. Applying the limits in (8) and the distribution function in (C2), (6) can be rewritten as

$$n_{\rm gen}=\frac{n_oB_se^{\frac{\Pi_o}{T_\parallel}}}{T_\perp\sqrt{\pi T_\parallel}}\int_{\mu_1}^{\mu_2}d\mu e^{\mu B_o\left(\frac{1}{T_\parallel}-\frac{1}{T_\perp}\right)} \tag{C3a}$$

$$\times\int_{\mu B_\alpha+\Pi_\alpha}^{\infty}dE\frac{e^{-\frac{E}{T_\parallel}}}{\sqrt{E-\mu B_s-\Pi_s}}$$

$$\phi_{\rm gen}=\frac{n_oB_se^{\frac{\Pi_o}{T_\parallel}}}{T_\perp}\sqrt{\frac{2}{\pi mT_\parallel}}\int_{\mu_1}^{\mu_2}d\mu\exp\left(\mu B_o\left(\frac{1}{T_\parallel}-\frac{1}{T_\perp}\right)\right) \tag{C3b}$$

$$\times\int_{\mu B_\alpha+\Pi_\alpha}^{\infty}dEe^{-\frac{E}{T_\parallel}}$$

$$P_{\parallel,\rm gen}=\frac{n_oB_se^{\frac{\Pi_o}{T_\parallel}}}{T_\perp\sqrt{\pi T_\parallel}}\int_{\mu_1}^{\mu_2}d\mu\exp\left(\mu B_o\left(\frac{1}{T_\parallel}-\frac{1}{T_\perp}\right)\right) \tag{C3c}$$

$$\times\int_{\mu B_\alpha+\Pi_\alpha}^{\infty}dE\sqrt{E-\mu B_s-\Pi_s}e^{-\frac{E}{T_\parallel}}$$

$$P_{\perp,\rm gen}=\frac{n_oB_s^2e^{\frac{\Pi_o}{T_\parallel}}}{T_\perp\sqrt{\pi T_\parallel}}\int_{\mu_1}^{\mu_2}d\mu\cdot\mu\exp\left(\mu B_o\left(\frac{1}{T_\parallel}-\frac{1}{T_\perp}\right)\right) \tag{C3d}$$

$$\times\int_{\mu B_\alpha+\Pi_\alpha}^{\infty}dE\frac{e^{-\frac{E}{T_\parallel}}}{\sqrt{E-\mu B_s-\Pi_s}}$$

$$\varepsilon_{\parallel,\rm gen}=\frac{n_oB_se^{\frac{\Pi_o}{T_\parallel}}}{T_\perp}\sqrt{\frac{2}{\pi mT_\parallel}}\int_{\mu_1}^{\mu_2}d\mu\exp\left(\mu B_o\left(\frac{1}{T_\parallel}-\frac{1}{T_\perp}\right)\right) \tag{C3e}$$

$$\times\int_{\mu B_\alpha+\Pi_\alpha}^{\infty}(E-\Pi_s)dEe^{-\frac{E}{T_\parallel}}$$

and the integrations can be carried out.

Because of the square root in the integrand of (C3a), (C3c), and (C3d), an error function will appear as part of the solution to this first integration over energy. The μ integration over this is straightforward, splitting the integrands into parts, and this yields an integration of the form

$$G\propto\int x^ae^{-yx^2}dx \tag{C4}$$

where a and y are real numbers. This integral has different solutions depending on the value of y such that

$$G(a,y)=\begin{cases}y=0: & \text{powers of } x\\ y>0: & \text{error functions}\\ y<0: & \text{Dawson integrals}\\ y\to\infty: & 0\end{cases} \tag{C5}$$

The final solution to the integrals is given in (9)-(11).

Appendix D: Regions of Integration and Comparison With *Lemaire and Scherer* [1971]

Here the various populations that are possible in the ionospheric outflow scenario with the generalization of (1) and (2) satified are discussed, along with a comparison of these results

with those of Lemaire and Scherer [1971] for the same conditions. *Lemaire and Scherer* [1971] defined the various classes of plasma populations as a function of velocity and pitch angle, v and θ, at an arbitrary spatial point s. These classes are shown in Figure 15 in $v_{||}$-$v_{\perp}$ space for decelerated and accelerated populations and are defined as follows: 1 (ballistic), decelerated ionospheric particles not reaching the upper simulation boundary; 2 (escaping), decelerated ionospheric particles reaching the upper boundary; 3 (incoming, not precipitating), downward-flowing magnetospheric particles accelerated by the potential structure that are magnetically mirrored before the ionospheric boundary and return to the magnetosphere; 4 (incoming, precipitating), downward-flowing accelerated magnetospheric particles that reach the ionosphere; 5 (trapped), particles that mirror before reaching either boundary that are reflected by the potential barrier and then mirrored back by the magnetic field; 6 (escaping), accelerated ionospheric particles, all of which reach the upper boundary; 7 (incoming, not precipitating), decelerated magnetospheric particles repelled before the ionosphere by the potential or the magnetic field and return to the magnetosphere; and 8 (incoming, precipitating), decelerated magnetospheric particles reaching the ionosphere. In Figure 15, then the velocity and pitch angle boundaries are as follows: θ_m is the curve separating particles that map to the ionospheric boundary from those that do not; the θ'_m curve separates those particles reaching the magnetospheric boundary from those that do not; v_b is the velocity at θ=90° separating regions 1 and 5; v_∞ is the velocity at θ=0° separating regions 1 and 2 (and 1 and 4); v_c is the velocity where θ_m and θ'_m intersect; v_d is the velocity at θ=90° that separates regions 3 and 5; and v_ψ is the velocity at θ=0° that separates regions 6 and 7 (and 7 and 8).

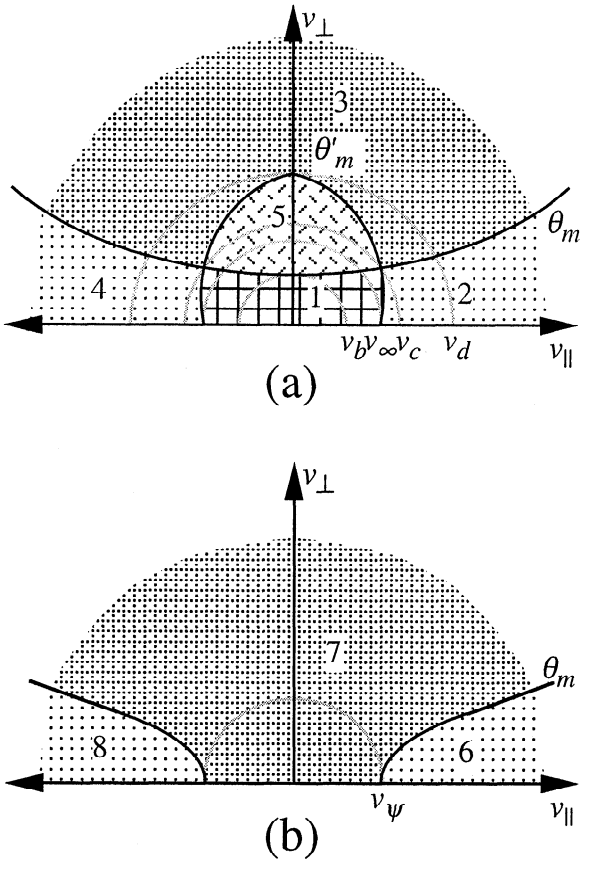

Figure 15. Schematic of the regions of $v_{||}$-$v_{\perp}$ space from *Lemaire and Scherer* [1971] for the classes described in Table 4 for (a) decelerated populations and (b) accelerated populations.

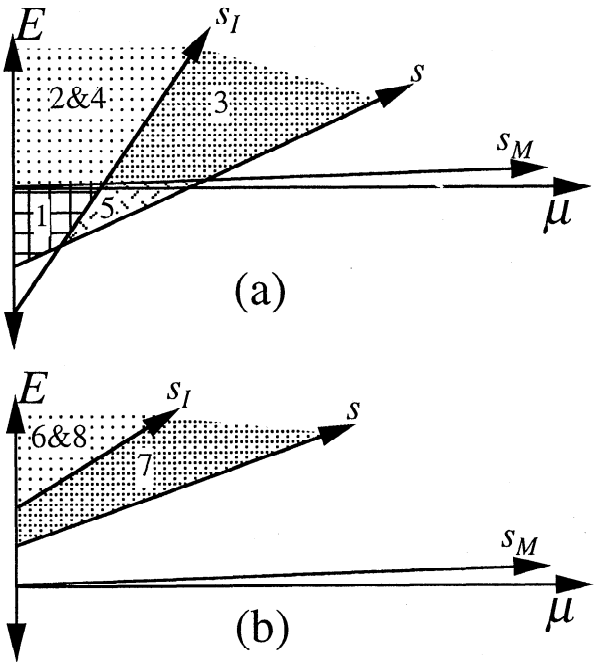

Figure 16. Schematic of the regions of E-μ space for the classes described in Table 4 for (a) decelerated populations and (b) accelerated populations. The s_α $v_{||}$=0 lines are $E=\mu B_\alpha+\Pi_\alpha$.

These classes and regions of velocity space can be described in E-μ space using the general formulation above. Figure 16 shows schematics of the regions of E-μ space for the classes shown in Figure 15. The corresponding limits and parameters that should be applied to (11) to reproduce these classes of particles are given in Table 4. The v and θ limits in Table 4 and Figure 15 can be written in terms of our variables as

$$\frac{mv_b^2}{2}=\frac{B_s}{B_I-B_s}(\Pi_s-\Pi_I)\qquad \frac{mv_\infty^2}{2}=\Pi_M-\Pi_s$$

$$\frac{mv_c^2}{2}=\frac{B_M}{B_I-B_M}(\Pi_M-\Pi_I)+\Pi_M-\Pi_s$$

$$\frac{mv_d^2}{2}=\frac{B_s}{B_s-B_M}(\Pi_M-\Pi_s)\qquad \frac{mv_\psi^2}{2}=\Pi_I-\Pi_s \tag{D1}$$

$$\sin^2\theta_m=\frac{B_s}{B_I}\left(\frac{E-\Pi_I}{E-\Pi_s}\right)\qquad \sin^2\theta'_m=\frac{B_s}{B_M}\left(\frac{E-\Pi_M}{E-\Pi_s}\right)$$

Note that θ_m and θ'_m map to straight lines in E-μ space (the ionospheric boundary (s_I) and magnetospheric boundary (s_M) $v_{||}$=0 lines, respectively), and the velocities map to energy differences (from Π_s) of the intersections of various $v_{||}$=0 lines. The α column shows the number of integrals needed to obtain the velocity moments for that class (that is, class 1 requires three general integration regions to be summed together, class 2 requires two, etc.). The column labeled f indicates the distri-

Table 4. *Lemaire and Scherer* [1971] Integration Regions Using the General Formulation

Class	v-θ Space Region, $\Sigma[v_{min},v_{max}]$; $[\theta_{min},\theta_{max}]$	α	B_α	Π_α	E-μ Space General Integrations μ_1	μ_2	f	+/-
	Decelerated $(\Pi_s - \Pi_o > 0)$							
1. Ballistic	$[0,v_b]$; $[0,\pi]$ and $[v_b,v_\infty]$; $[0,\theta_m]$	1	B_s	Π_s	0	$\frac{\Pi_s-\Pi_I}{B_I-B_s}$	$f_I^+ + f_I^-$	+
	and $[v_b,v_\infty]$; $[\pi-\theta_m,\pi]$	2	B_I	Π_I	$\frac{\Pi_s-\Pi_I}{B_I-B_s}$	$\frac{\Pi_M-\Pi_I}{B_I-B_M}$	$f_I^+ + f_I^-$	+
	and $[v_\infty,v_c]$; $[\theta'_m,\theta_m]$	3	B_M	Π_M	0	$\frac{\Pi_M-\Pi_I}{B_I-B_M}$	$f_I^+ + f_I^-$	-
	and $[v_\infty,v_c]$; $[\pi-\theta_m,\pi-\theta'_m]$							
2. Escaping	$[v_\infty,v_c]$; $[0,\theta'_m]$ and $[v_c,\infty]$; $[0,\theta_m]$	1	B_M	Π_M	0	$\frac{\Pi_M-\Pi_I}{B_I-B_M}$	f_I^+	+
		2	B_I	Π_I	$\frac{\Pi_M-\Pi_I}{B_I-B_M}$	∞	f_I^+	+
3. Incoming	$[v_c,v_d]$; $[\theta_m,\theta'_m]$	1	B_M	Π_M	$\frac{\Pi_M-\Pi_I}{B_I-B_M}$	$\frac{\Pi_M-\Pi_s}{B_s-B_M}$	$f_M^+ + f_M^-$	+
(reflected)	and $[v_c,v_d]$; $[\pi-\theta'_m,\pi-\theta_m]$	2	B_s	Π_s	$\frac{\Pi_M-\Pi_s}{B_s-B_M}$	∞	$f_M^+ + f_M^-$	+
	and $[v_d,\infty]$; $[\theta_m,\pi-\theta_m]$	3	B_I	Π_I	$\frac{\Pi_M-\Pi_I}{B_I-B_M}$	∞	$f_M^+ + f_M^-$	-
4. Incoming	$[v_\infty,v_c]$; $[\pi,\pi-\theta'_m]$ and $[v_c,\infty]$; $[\pi-\theta_m,\pi]$	1	B_M	Π_M	0	$\frac{\Pi_M-\Pi_I}{B_I-B_M}$	f_M^-	+
(precipitating)		2	B_I	Π_I	$\frac{\Pi_M-\Pi_I}{B_I-B_M}$	∞	f_M^-	+
5. Trapped	$[v_b,v_\infty]$; $[\theta_m,\pi-\theta_m]$	1	B_s	Π_s	$\frac{\Pi_s-\Pi_I}{B_I-B_s}$	$\frac{\Pi_M-\Pi_s}{B_s-B_M}$	$f_T^+ + f_T^-$	+
	and $[v_\infty,v_d]$; $[\theta'_m,\pi-\theta'_m]$	2	B_I	Π_I	$\frac{\Pi_s-\Pi_I}{B_I-B_s}$	$\frac{\Pi_M-\Pi_I}{B_I-B_M}$	$f_T^+ + f_T^-$	-
		3	B_M	Π_M	$\frac{\Pi_M-\Pi_I}{B_I-B_M}$	$\frac{\Pi_M-\Pi_s}{B_s-B_M}$	$f_T^+ + f_T^-$	-
	Accelerated $(\Pi_s - \Pi_o < 0)$							
6. Escaping	$[v_\psi,\infty]$; $[0,\theta_m]$	1	B_I	Π_I	0	∞	f_I^+	+
7. Incoming	$[0,v_\psi]$; $[0,\pi]$ and $[v_\psi,\infty]$; $[\theta_m,\pi-\theta_m]$	1	B_s	Π_s	0	∞	$f_M^+ + f_M^-$	+
(reflected)		2	B_I	Π_I	0	∞	$f_M^+ + f_M^-$	-
8. Incoming (precipitating)	$[v_\psi,\infty]$; $[\pi-\theta_m,\pi]$	1	B_I	Π_I	0	∞	f_M^-	+

bution function that should be used. Here the plus and minus superscripts indicate upward and downward flowing particles, respectively; f_I is the distribution of the outflowing ionospheric particles at the ionospheric boundary s_I; f_M is the distribution of the incoming magnetospheric particles at the magnetospheric boundary s_M; and f_T is the distribution of the trapped particles, defined at some intermediate reference point. Note that the reference point s_o in (9)-(11) should change for each population, accordingly, and that f^+ and f^- will subtract instead of add in (9b) and (9e). The final column indicates whether this integral should be added (+) or subtracted (-) from the calculation. The subtractions are necessary to omit filled regions counted as part of another population. It should also be stressed that all of the Π quantities are population-specific due to the charge and mass dependencies of the potential energies.

To illustrate the use of this table, ballistic particles (class 1) require three general integration regions above $v_{||}$=0 lines to be summed together: above the local point's line from μ=0 until it intersects the s_I line; above the s_I line until it intersects the s_M line; and then above the s_M line from zero to its intersection with the s_I line. The last of the three integrals should be subtracted rather than added to the others. These three lines define the checked region in Figures 15a and 16a.

To obtain the formulation presented by *Lemaire and Scherer* [1971], the integrals defined in Table 4 must be applied to (9)

with A=0. For example, the integration for class 2 (escaping decelerated particles) is defined by two general integrals, and the resulting formulas are

$$n = n_{o,I} e^{\frac{\Pi_I - \Pi}{T}} \left\{ \mathrm{erfc}\left(\sqrt{\frac{\Pi_M - \Pi}{T}}\right) - \sqrt{\frac{B_I - B}{B_I}} \times \exp\left(\frac{B}{B_I - B}\frac{\Pi_I - \Pi}{T}\right)\mathrm{erfc}\left(\sqrt{\frac{B}{B_I - B}x}\right) + \frac{2}{\sqrt{\pi}}\sqrt{\frac{B - B_M}{B_M}}\exp\left(\frac{B}{B_M - B}\frac{\Pi_M - \Pi}{T}\right) \times \left[\exp\left(\frac{B_M}{B - B_M}\frac{\Pi_M - \Pi}{T}\right) D\left(\sqrt{\frac{B_M}{B - B_M}\frac{\Pi_M - \Pi}{T}}\right) - exp\left(\frac{B_M}{B - B_M}x\right) D\left(\sqrt{\frac{B_M}{B - B_M}x}\right)\right]\right\} \quad \text{(D2)}$$

$$\phi = n_{o,I}\sqrt{\frac{2T}{\pi m}}\frac{B}{B_M} e^{\frac{\Pi_I - \Pi_M}{T}} \times \left\{1 - \frac{B_I - B_M}{B_I}\exp\left(\frac{B_M}{B_I - B_M}\frac{\Pi_I - \Pi_M}{T}\right)\right\} \quad \text{(D3)}$$

$$P_{||} = nT + n_{o,I}Te^{\frac{\Pi_I - \Pi}{T}}\left\{e^{\frac{B}{B_I - B}\frac{\Pi_I - \Pi}{T}}\frac{B}{B_I}\left[\sqrt{\frac{B_I - B}{B_I}} \times \mathrm{erfc}\left(\sqrt{\frac{B_I}{B_I - B}x}\right) + \sqrt{\frac{x}{\pi}}\exp\left(-\frac{B_I}{B_I - B}x\right)\right] - \exp\left(\frac{B}{B_M - B}\frac{\Pi_M - \Pi}{T}\right)\frac{1}{\sqrt{\pi}}\frac{B}{B_M} \times \left[\exp\left(\frac{B_M}{B - B_M}x\right)\left(\sqrt{\frac{B - B_M}{B_M}} D\left(\sqrt{\frac{B_M}{B - B_M}x}\right) - \sqrt{x}\right)\right. \right. - \exp\left(\frac{B_M}{B - B_M}\frac{\Pi_M - \Pi}{T}\right)\left(\sqrt{\frac{B - B_M}{B_M}} \left. \left. \times D\left(\sqrt{\frac{B_M}{B - B_M}\frac{\Pi_M - \Pi}{T}}\right) - \sqrt{\frac{\Pi_M - \Pi}{T}}\right)\right]\right\} \quad \text{(D4)}$$

$$P_{\perp} = P_{||} + n_{o,I}Te^{\frac{\Pi_I - \Pi}{T}}\left\{\frac{\Pi_I - \Pi}{T}\exp\left(\frac{B}{B_I - B}\frac{\Pi_I - \Pi}{T}\right) \times \frac{B}{B_I}\sqrt{\frac{B_I}{B_I - B}}\mathrm{erfc}\left(\sqrt{\frac{B_I}{B_I - B}x}\right) + \frac{\Pi_M - \Pi}{T} \times \exp\left(\frac{B}{B_M - B}\frac{\Pi_M - \Pi}{T}\right)\frac{B}{B_M}\sqrt{\frac{B_M}{B - B_M}} \times \left[\exp\left(\frac{B_M}{B - B_M}\frac{\Pi_M - \Pi}{T}\right)\right. \left. \times D\left(\sqrt{\frac{B_M}{B - B_M}\frac{\Pi_M - \Pi}{T}}\right) - e^{\frac{B_M}{B - B_M}x} D\left(\sqrt{\frac{B_M}{B - B_M}x}\right)\right]\right\} \quad \text{(D5)}$$

$$\varepsilon_{||} = n_{o,I}T\sqrt{\frac{2T}{\pi m}}\frac{B}{B_M}e^{\frac{\Pi_I - \Pi_M}{T}}\left\{2 + \frac{\Pi_M - \Pi}{T} - \left[\frac{B_M}{B_I}\frac{\Pi_I - \Pi_M}{T} + \frac{B_I - B_M}{B_I}\left(2 + \frac{\Pi_M - \Pi}{T}\right) \times \exp\left(\frac{B_M}{B_I - B_M}\frac{\Pi_I - \Pi_M}{T}\right)\right]\right\} \quad \text{(D6)}$$

using the notation of section 4, with

$$x = \frac{B_I - B}{B_I - B_M}\frac{\Pi_M - \Pi_I}{T} + \frac{\Pi_I - \Pi}{T} \quad \text{(D7)}$$

These are the same equations as (17)-(19) of *Lemaire and Scherer* [1971], where their shorthand notations can be written in terms of our variables as

$$p = \frac{B_I - B}{B_I} \quad \sigma = \frac{B - B_M}{B_M} \quad q = \frac{\Pi - \Pi_I}{T} \quad V_\infty^2 = \frac{\Pi_M - \Pi}{T} \quad X^2 = x \quad \text{(D8)}$$

The other classes of particles discussed by them can also be compared with this model by applying (9) for the appropriate regions from Table 4 and converting the two sets of equations to a common set of variables.

Appendix E: Timescale Comparison

The use of the first adiabatic invariant μ implies a gyration-averaged kinetic equation, and this is only valid if the gyroperiod is the shortest timescale of the processes acting on the plasma. To verify that this is true, the gyroperiod τ_B must be compared with the timescale for the change in velocity due to the parallel force acting on the particles τ_F,

$$\tau_F = \frac{m\bar{v}}{eF_{||}} \quad \text{(E1)}$$

$$\tau_B = \frac{1}{2\pi\omega_B} = \frac{m}{2\pi eB} \quad \text{(E2)}$$

where $\bar{v}$ is the average speed of the population. Replacing $E_{||}$ with $-\Delta\Pi/\Delta s$, the potential difference per unit length, leads to the condition

$$\Delta\Pi << \bar{v}B\Delta s \quad \text{(E3)}$$

For the outflow of oxygen ions from the high-latitude ionosphere, most of the potential drop occurs near the ionospheric boundary, yielding a constraint of

$$\Delta\Pi << 2\pi\left(10^3\ \mathrm{m/s}\right)\left(5\times10^{-5}\ \mathrm{T}\right)\left(10^6\ \mathrm{m}\right) \cong 3\times10^5\ \mathrm{V} \quad \text{(E4)}$$

which is easily met for the potential differences along high-latitude field lines (typically a few volts up to tens of volts). This limiting potential drop will be even higher for the lighter species.

Magnetospherically trapped hot plasma can also be tested using (E3). In this scenario, most of the potential drop occurs near the equatorial plane, yielding (for hot protons with 25 keV of thermal energy [*Miller and Khazanov*, 1993])

$$\Delta\Pi << 2\pi\left(2\times10^6\ \mathrm{m/s}\right)\left(10^{-7}\ \mathrm{T}\right)\left(6\times10^6\ \mathrm{m}\right) \cong 8\times10^6\ \mathrm{V} \quad \text{(E5)}$$

This number is much greater than the potential drops affecting such a population (as discussed in section 5.1). So the constraint is met for this situation, and the guiding center approximation (and thus the use of μ) is justified.

Acknowledgments. This work was funded by the National Science Foundation under grants ATM-9523699 and ATM-9710326. M. W. Liemohn held a National Research Council Resident Research Associateship at Marshall Space Flight Center while this work was performed.

The Editor thanks H. G. Demars and T. J. Birmingham for their assistance in evaluating this paper.

References

Alfvén, H., and C.-G. Fälthammar, *Cosmical Electrodynamics, Fundamental Principles*, Oxford Univ. Press, New York, 1963.

Barakat, A. R., and R. W. Schunk, Effect of the hot electrons on the polar wind, *J. Geophys. Res.., 89*, 9771, 1984.

Birn, J., M. F. Thomsen, J. E. Borovsky, G. D. Reeves, D. J. McComas, and R. D. Belian, Characteristic plasma properties during dispersionless substorm injections at geosynchronous orbit, *J. Geophys. Res., 102*, 2309, 1997.

Chiu, Y. T., and M. Schulz, Self-consistent particle and parallel electrostatic field distributions in the magnetospheric-ionospheric auroral region, *J. Geophys. Res., 83*, 629, 1978.

Eviatar, A., A. M. Lenchek, and S. F. Singer, Distribution of density in an ion-exosphere of a non-rotating planet, *Phys. Fluids, 7*, 1775, 1964.

Guglielmi, A., J. Kangas, K. Mursula, T. Pikkarainen, O. Pokhotelov, and A. Potapov, Pc 1 induced electromagnetic lift of background plasma in the magnetosphere, *J. Geophys. Res., 101*, 21,493, 1996.

Horwitz, J. L., C. W. Ho, H. D. Scarbro, G. R. Wilson, and T. E. Moore, Centrifugal acceleration of the polar wind, *J. Geophys. Res., 99*, 15,051, 1994.

Huang, T. S., and T. J. Birmingham, The polarization electric field and its effects in an anisotropic rotating magnetospheric plasma, *J. Geophys. Res., 97*, 1511, 1992.

Khazanov, G. V., M. W. Liemohn, and T. E. Moore, Photoelectron effects on the self-consistent potential in the collisionless polar wind, *J. Geophys. Res., 102*, 7509, 1997.

Knight, S., Parallel electric fields, *Planet. Space Sci., 21*, 741, 1973.

Lemaire, J., Rotating ion exospheres, *Planet. Space Sci., 24*, 975, 1976.

Lemaire, J., and M. Scherer, Model of the polar ion-exosphere, *Planet. Space Sci., 18*, 103, 1970.

Lemaire, J., and M. Scherer, Simple model for an ion-exosphere in an open magnetic field, *Phys. Fluids, 14*, 1683, 1971.

Lemaire, J., and M. Scherer, Ion-exosphere with asymmetric velocity distribution, *Phys. Fluids, 15*, 760, 1972.

Lemaire, J., and M. Scherer, Plasma sheet particle precipitation: A kinetic model, *Planet. Space Sci., 21*, 281, 1973.

Lemaire, J., and M. Scherer, Ionosphere-plasmasheet field-aligned currents and parallel electric fields, *Planet. Space Sci., 22*, 21485, 1974.

Li, X., and M. Temerin, Ponderomotive effects on ion acceleration in the auroral zone, *Geophys. Res. Lett., 20*, 13, 1993.

Liemohn, M. W., and G. V. Khazanov, Nonsteady-state coupling processes in superthermal electron transport, in *Cross-Scale Coupling in Space Plasmas, Geophys. Monogr. Ser.*, vol. 93, edited by J. L. Horwitz, N. Singh, and J. L. Burch, p. 181-191, AGU, Washington, D. C., 1995.

Liemohn, M. W., and G. V. Khazanov, Collisionless plasma modeling in an arbitrary potential energy distribution, *Phys. Plas.*, in press, 1998.

Liemohn, M. W., G. V. Khazanov, T. E. Moore, and S. M. Guiter, Self-consistent superthermal electron effects on plasmaspheric refilling, *J. Geophys. Res., 102*, 7523, 1997a.

Liemohn, M. W., G. V. Khazanov, and E. N. Krivorutsky, Self-consistent effects of superthermal electrons and a trapped hot population on plasmaspheric refilling (abstract), *Eos Trans. AGU*, 78(17), Spring Meet. Suppl., S286, 1997b.

Lundin, R., and B. Hultqvist, Ionospheric plasma escape by high-latitude electric fields: Magnetic moment "pumping," *J. Geophys. Res., 94*, 6665, 1989.

Lyons, L. R., and D. J. Williams, *Quantitative Aspects of Magnetospheric Physics*, Reidel, Norwell, Mass., 1984.

Miller, R. H., and G. V. Khazanov, Self-consistent electrostatic potential due to trapped plasma in the magnetosphere, *Geophys. Res. Lett., 20*, 1331, 1993.

Olsen, R. C., L. J. Scott, and S. A. Boardsen, Comparison between Liouville's theorem and observed latitudinal distributions of trapped ions in the plasmapause region, *J. Geophys. Res., 99*, 2191, 1994.

Persson, H., Electric field along a magnetic field line of force in a low-density plasma, *Phys. Fluids, 6*, 1756, 1963.

Pierrard, V., and J. Lemaire, Lorentzian ion exosphere model, *J. Geophys. Res., 101*, 7923, 1996.

Richards, P. G., J. A. Fennelly, and D. G. Torr, EUVAC: A solar EUV flux model for aeronomic calculations, *J. Geophys. Res., 99*, 8981, 1994.

Serizawa, Y., and T. Sato, Generation of large-scale potential difference by currentless plasma jets along the mirror field, *Geophys. Res. Lett., 11*, 595, 1984.

Singh, N., and J. L. Horwitz, Plasmaspheric refilling, *J. Geophys. Res., 97*, 1049, 1992.

Stasiewicz, K., The influence of a turbulent region on the flux of auroral electrons, *Planet. Space Sci., 6*, 591, 1985.

Tam, S. W. Y., F. Yasseen, and T. Chang, Self-consistent kinetic photoelectron effects on the polar wind, *Geophys. Res. Lett., 22*, 2107, 1995.

Washimi, H., and I. Katanuma, Numerical BGK-solutions of large scale electrostatic potential in auroral plasmas, *Geophys. Res. Lett., 13*, 897, 1986.

Whipple, E. C., The signature of parallel electric fields in a collisionless plasma, *J. Geophys. Res., 82*, 1525, 1977.

Wilson, G. R., G. V. Khazanov, and J. L. Horwitz, Achieving zero current for polar wind outflow on open flux tubes subjected to large photoelectron fluxes, *Geophys. Res. Lett., 24*, 1183, 1997.

G. V. Khazanov and E. N. Krivorutsky, Center for Space Physics and Aeronomic Research, The University of Alabama in Huntsville, Huntsville, AL 35899 (george.khazanov@msfc.nasa.gov).

M. W. Liemohn, Space Sciences Laboratory, NASA Marshall Space Flight Center, Code ES-83, Huntsville, AL 35812 (mike.liemohn@msfc.nasa.gov).

T. E. Moore, Laboratory for Extraterrestrial Physics, NASA Goddard Space Flight Center, Code 692, Greenbelt, MD 20771 (Thomas.E.Moore@GSFC.NASA.gov).

(Received August 26, 1997; revised November 20, 1997; accepted November 21, 1997.)